

## The Global Ozone Monitoring Experiment (GOME): Mission Concept and First Scientific Results

JOHN P. BURROWS, MARK WEBER, MICHAEL BUCHWITZ, VLADIMIR ROZANOV,  
ANNETTE LADSTÄTTER-WEIßENMAYER, ANDREAS RICHTER, RÜDIGER DEBEEK, RICARDA HOOGEN,  
KLAUS BRAMSTEDT, KAI-UWE EICHMANN, AND MICHAEL EISINGER\*

*Institute of Environmental Physics, University of Bremen, Bremen, Germany*

DIETER PERNER

*Max Planck Institute for Chemistry, Mainz, Germany*

(Manuscript received 4 September 1997, in final form 19 June 1998)

### ABSTRACT

The Global Ozone Monitoring Experiment (GOME) is a new instrument aboard the European Space Agency's (ESA) *Second European Remote Sensing Satellite (ERS-2)*, which was launched in April 1995. The main scientific objective of the GOME mission is to determine the global distribution of ozone and several other trace gases, which play an important role in the ozone chemistry of the earth's stratosphere and troposphere. GOME measures the sunlight scattered from the earth's atmosphere and/or reflected by the surface in nadir viewing mode in the spectral region 240–790 nm at a moderate spectral resolution of between 0.2 and 0.4 nm. Using the maximum 960-km across-track swath width, the spatial resolution of a GOME ground pixel is  $40 \times 320$  km<sup>2</sup> for the majority of the orbit and global coverage is achieved in three days after 43 orbits.

Operational data products of GOME as generated by DLR-DFD, the German Data Processing and Archiving Facility (D-PAF) for GOME, comprise absolute radiometrically calibrated earthshine radiance and solar irradiance spectra (level 1 products) and global distributions of total column amounts of ozone and NO<sub>2</sub> (level 2 products), which are derived using the DOAS approach (Differential Optical Absorption Spectroscopy). (Under certain conditions and some restrictions, the operational data products are publically available from the European Space Agency via the ERS Helpdesk.)

In addition to the operational data products, GOME has delivered important information about other minor trace gases such as OCIO, volcanic SO<sub>2</sub>, H<sub>2</sub>CO from biomass burning, and tropospheric BrO. Using an iterative optimal estimation retrieval scheme, ozone vertical profiles can be derived from the inversion of the UV/VIS spectra. This paper reports on the GOME instrument, its operation mode, and the retrieval techniques, the latter with particular emphasis on DOAS (total column retrieval) and advanced optimal estimation (ozone profile retrieval).

Observation of ozone depletion in the recent polar spring seasons in both hemispheres are presented. OCIO observed by GOME under twilight conditions provides valuable information on the chlorine activation inside the polar vortex, which is believed to be responsible for the rapid catalytic destruction of ozone. Episodes of enhanced BrO in the Arctic, most likely contained in the marine boundary layer, were observed in early and late spring. Excess tropospheric nitrogen dioxide and ozone have been observed during the recent Indonesian fire in fall 1997. Formaldehyde could also clearly be identified by GOME and is known to be a by-product resulting from biomass burning.

### 1. Introduction

Dramatic changes in atmospheric composition causing a severe depletion of ozone during the Antarctic spring first detected by Farman et al. (1985) and their

global impact (Houghton et al. 1991) established the need for global measurements of trace atmospheric constituents (ESA 1991). The SCIAMACHY (Scanning Imaging Absorption Spectrometer for Atmospheric Cartography) instrument proposal (Burrows et al. 1988a; Bovensmann et al. 1999) was prepared in response to an ESA (European Space Agency) call for instrumentation to fly on its polar orbiting platform, now known as ENVISAT-1 (First European Environmental Satellite), which is due for launch in 2000. In late 1988 it was recognized that an instrument for global monitoring of ozone and other trace gases should be added as the only new instrument to the *Second European Remote Sensing Satellite (ERS-2)* mission in order to satisfy the

---

\* Current affiliation: Alfred Wegener Institute for Polar and Marine Research, Potsdam, Germany

---

Corresponding author address: Dr. Mark Weber, Institute of Environmental Physics, University of Bremen, P.O. Box 330440, D-28203 Bremen, Germany.  
E-mail: mark.weber@iup.physik.uni-bremen.de

need for global trace constituent measurements as soon as possible prior to the launch of ENVISAT-1. In response to an ESA announcement of opportunity, SCIAMACHY scientists proposed a small-scale version of SCIAMACHY under the name SCIAMini (Burrows et al. 1988b), which after some modification was renamed the Global Ozone Monitoring Experiment (GOME) and approved by the ESA council to be launched aboard ERS-2 in June 1990 (ESA 1993).

GOME measures the earthshine radiance and the solar irradiance in the UV/VIS spectral range 240–790 nm at a moderate spectral resolution of 0.2–0.4 nm. Trace gas total column amounts are retrieved from these primary measurements utilizing their characteristic spectral absorption (e.g., the ozone Huggins and Chappuis bands) or emission features (e.g., NO  $\gamma$  bands). The large spectral range of GOME combined with the high spectral resolution permits the application of the DOAS (Differential Optical Absorption Spectroscopy) algorithm to the retrieval of column amounts of many trace gases (e.g., Noxon et al. 1979; Platt 1994 and references therein). The DOAS technique utilizes the differential structure of the absorption bands, to which a linear combination of molecular reference spectra are matched after subtracting the broad spectral background due to scattering processes, surface albedo, and the slowly varying components of absorption. The DOAS method has been successfully applied to ground-based, aircraft, and balloon-borne measurements for several years. GOME, however, is the first instrument employing this technique from space for the derivation of trace gas abundance.

Ozone vertical profiles can be derived by inversion of the radiance measurements between 240 and 400 nm using algorithms similar to those developed for NASA's Solar Backscatter UV (SBUV) instruments (Barthia et al. 1996). Cloud information can be obtained from the spectral reflectance measurements inside and outside the oxygen bands (cloud cover). Surface and aerosol information can be retrieved from their broadband effects on the upwelling radiance.

The measurement and retrieval objectives of the GOME mission can be grouped as follows (Burrows et al. 1990; Burrows and Chance 1993; ESA 1993):

- 1) *Radiation measurements*: the solar irradiance, the earthshine radiance or nadir spectrum, and lunar spectra (Dobber 1997; Dobber et al. 1998) in the spectral range 240–790 nm.
- 2) *Trace gas retrieval*: global measurements of total columns of O<sub>3</sub>, NO<sub>2</sub>, BrO, H<sub>2</sub>O, O<sub>4</sub>, O<sub>2</sub>, and NO<sub>3</sub>; OClO and ClO (under ozone hole conditions), NO (above 40 km), SO<sub>2</sub> (under polluted conditions and following volcanic eruptions), H<sub>2</sub>CO (under polluted conditions), and ozone vertical profiles.
- 3) *Clouds*: cloud cover, cloud reflectance, and possibly cloud-top height and optical depth.

- 4) *Surface properties*: albedo and surface spectral reflectance.
- 5) *Aerosols*: aerosol vertical optical depth and type.
- 6) *Solar UV irradiance variability*: observation of solar UV flux variation related to the 11-year solar cycle (Weber et al. 1998).

This paper mainly concentrates on the total column retrieval of selected atmospheric molecules and the ozone profile retrieval (2) and only some aspects of (1), (2), and (4) are considered, which are relevant to the trace gas retrieval.

The purpose of this paper is to give a comprehensive overview of the GOME instrument and its measurement modes, the retrieval techniques to derive total columns of trace gases (DOAS) and ozone profiles (advanced optimal estimation). Some of the major scientific achievements from the global measurements during its first three years of operation in space are presented. A brief description of the GOME instrument and its measurement modes is given in section 2. Relevant aspects of the GOME operational ground segment, such as the operational level 0 to 1 (radiometric calibration of spectral data) and level 1 to 2 processing (DOAS retrieval of O<sub>3</sub> and NO<sub>2</sub> trace gas amounts and cloud correction) algorithms, which are executed at the DFD/DLR (German Remote Sensing Data Center of the DLR), the German Data Processing and Archiving Facility (D-PAF) of GOME, are discussed in section 3. The most important modifications to the GOME operation and data processing resulting from the geophysical validation phase (April 1995–June 1996) following the launch of ERS-2 on 21 April 1995 are also briefly described in section 3c. Selected GOME ozone distributions measured in the Antarctic (1995–97) and Arctic (1996–98) spring seasons, and a one-year total climatology of total ozone are shown in section 4c. As an example of additional research products from GOME, DOAS trace gas retrieval of stratospheric OClO over Antarctica in 1995 (section 5a), tropospheric BrO in the Arctic (section 5b), tropospheric SO<sub>2</sub> from the volcanic eruption of Nyamuragira in Zaire in December 1996 (section 5c), and GOME detection of biomass burning during the Indonesian fires in fall 1997 (section 5d) are presented. Finally, the GOME ozone profile retrieval based upon an advanced optimal estimation method and first results from the Arctic winter campaign in 1997 are presented in section 6.

## 2. GOME instrument

### a. GOME spectrometer

The GOME instrument is a double monochromator that combines a predisperser prism and a grating in each of the four channels as dispersing elements. A schematic diagram of the GOME optical layout is shown in Fig. 1. Except for the scan mirror at the nadir view port, all spectrometer parts are fixed and the spectra are recorded

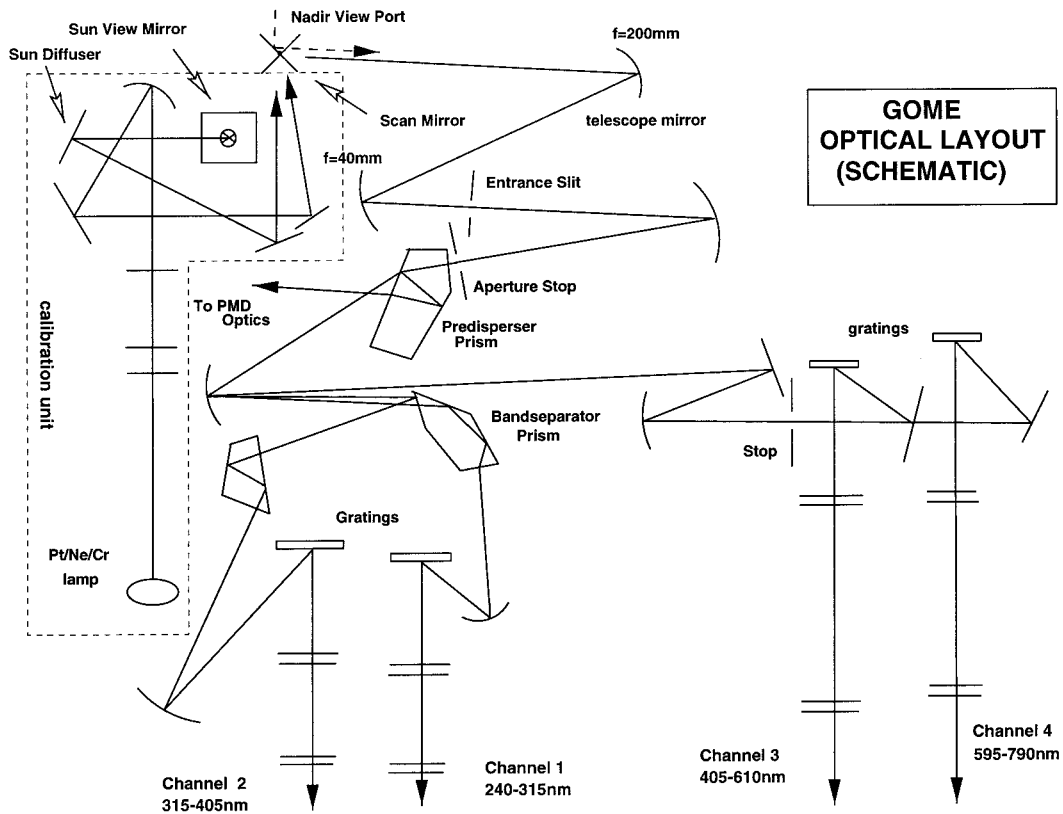


FIG. 1. Schematic instrumental setup of GOME. The GOME instrument is a four-channel spectrometer. Attached to the spectrometer is a calibration unit housing a Pt/Cr/Ne hollow cathode discharge lamp and the fore optics for solar viewing. Not shown is an additional mirror, which directs the lamp light to the solar diffuser plate for diffuser reflectivity monitoring.

simultaneously from 240 to 790 nm. In the nadir observation mode (and when observing the moon) light enters GOME via the nadir scan mirror and is focused onto the entrance slit of the spectrometer by an anamorphic telescope formed by two cylindrical mirrors. The instantaneous field of view (IFoV) is  $2.9^\circ \times 0.14^\circ$ , corresponding to an area of about  $40 \times 2 \text{ km}^2$  on the earth's surface (with the longer dimension parallel to the flight direction, i.e., perpendicular to the scan direction). In order to cover the broad spectral range with the required resolution, light entering GOME is split into four separate spectral bands by a predisperser prism, a channel separator prism, and a beam splitter. In each of the four spectral channels, the light is dispersed by a diffraction grating and focused onto a monolithic silicon linear detector array (Reticon RL1024) comprising 1024 individual detector pixels.

In order to reduce the dark current and to improve the signal-to-noise ratio the detectors are maintained at 235 K by Peltier coolers that are connected to passive deep space radiators. To correct for effects caused by the polarization sensitivity of GOME a small fraction of light polarized perpendicular to the main optical plane (parallel to the entrance slit) is reflected off the predisperser prism toward dedicated polarization measurement devices (PMDs), which are three fast broadband silicon diodes whose spectral range covers approximately the optical channels 2 (300–400 nm), 3 (400–580 nm), and 4 (580–750 nm), respectively. The primary purpose of the PMDs is to determine the fractional polarization of the incoming backscattered radiation with respect to an instrument-defined plane, assuming that the polarization sensitivity of the optical components is known from preflight calibration measurements. Almost all onboard calibration facilities (except the LEDs, which illuminate the detector arrays to monitor the pixel-to-pixel variability) are contained in a dedicated calibration unit, housing the Pt/Cr/Ne hollow cathode gas discharge lamp (spectral wavelength calibration) and the sun viewport consisting of diffuser plate, sun view mirror, shutter, and a 20% transmission mesh. The main features of GOME are summarized in Table 1.

During the preflight calibration phase, the spectral irradiance of the GOME flight model was calibrated by the TPD-TNO in Delft using a 1000-watt FEL lamp, which in turn was referenced to an absolute standard at the National Institute of Standard and Technology (NIST). The absolute accuracy of the NIST standard is

During the preflight calibration phase, the spectral irradiance of the GOME flight model was calibrated by the TPD-TNO in Delft using a 1000-watt FEL lamp, which in turn was referenced to an absolute standard at the National Institute of Standard and Technology (NIST). The absolute accuracy of the NIST standard is

TABLE 1. Main features of the GOME spectrometer aboard *ERS-2*.

GOME/ <i>ERS-2</i>	
Spectrometer type	Double monochromator with predisperser prism and four holographic gratings (four channels)
Detectors	Four Reticon Si diode arrays ( $4 \times 1024$ pixels) Channel 1A 237–307 nm (IT = 12 s, RES = 0.20 nm) Channel 1B 307–315 nm (IT = 1.5 s, RES = 0.20 nm) Channel 2 312–406 nm (IT = 1.5 s, RES = 0.17 nm) Channel 3 397–609 nm (IT = 1.5 s, RES = 0.29 nm) Channel 4 576–794 nm (IT = 1.5 s, RES = 0.33 nm) Three Polarization Measuring Devices (PMD) (IT = 93.5 msec) PMD1 295–397-nm band PMD2 397–580-nm band PMD3 580–745-nm band
<i>ERS-2</i> orbit	Retrograde near polar ( $98.5^\circ$ inclination), sun-synchronous, descending node (equator crossing 1030 LST). 795-km altitude.
Viewing modes	<ul style="list-style-type: none"> <li>● Nadir (across-track scan angle <math>\pm 32^\circ</math>)</li> <li>● polar viewing (polar summer, <math>47^\circ</math> scan angle)</li> <li>● solar viewing (once a day)</li> <li>● lunar viewing (<math>\sim 6</math> times per year, <math>75^\circ</math>–<math>85^\circ</math> scan angle)</li> <li>● Pt–Ne–Cr hollow cathode discharge lamp <ul style="list-style-type: none"> <li>— wavelength calibration</li> <li>— diffuser plate degradation monitoring</li> </ul> </li> <li>● telescope (dark current, LED measurements)</li> </ul>
Spatial resolution/ $\approx$ nadir	$40 \times 320$ km <sup>2</sup> (IT = 1.5 s) $\approx 100 \times 960$ km <sup>2</sup> (IT = 12 s) $40 \times 20$ km <sup>2</sup> (PMD)
Major absorber	O <sub>3</sub> , NO <sub>2</sub> , O <sub>2</sub> , O <sub>4</sub> , H <sub>2</sub> O
Minor absorber	BrO, OClO, SO <sub>2</sub> , H <sub>2</sub> CO, NO (in emission) (tentatively: ClO, NO <sub>3</sub> , IO, OBrO)
Other data	clouds, aerosols, surface reflectivity, polarization, solar variability, UV index

quoted to be 1%–3% in the range 250–340 nm. The bidirectional reflection distribution function of the diffuser plate as a function of the solar azimuth and elevation angle has also been characterized during the pre-flight activities. The 1000-W FEL lamp combined with a spectralon diffuser plate placed in front of the nadir viewport served as a radiance standard. The performance of the spectralon diffuser plate has been compared with the NASA integrating sphere that has been used as a radiance standard to the Shuttle SBUV instruments and the agreement is within 1% (ESA 1995,

76). The scan mirror angle dependency of the radiance response function was taken into account.

### b. Measurement modes

On 21 April 1995 *ERS-2* was launched from Kourou, French Guyana, into a near-polar sun-synchronous orbit at a mean altitude of 785 km. After outgassing in orbit for approximately one month, GOME was cooled down and activated, and routine measurements began on 28 June 1995. During the illuminated part of the orbit, GOME performs nadir observation of the earth by scanning the surface from east ( $-30^\circ$ ) to west ( $+30^\circ$ ) and back, while *ERS-2* moves  $7 \text{ km s}^{-1}$  on the descending node with a mean local equator crossing time of 1030 LST. One across-track scan cycle of GOME lasts 6 s, 4.5 s for the forward scan, and 1.5 s for the backscan. Assuming a nominal integration time of 1.5 s for the GOME spectra, the forward scan, therefore, consists of three GOME ground pixels with an area coverage of  $40 \times 320 \text{ km}^2$  each for the maximum possible swath width of 960 km. As *ERS-2* is in a sun-synchronous near-polar orbit, nadir viewing results in a gap over the poles. During the polar summers a sideways polar viewing mode, where the scan mirror is then statically positioned at about an  $47^\circ$  angle from the nadir direction, is introduced. Using the maximum scan width GOME achieves global coverage at the equator within three days (43 orbits) and faster at higher latitudes.

Due to the large dynamic range of the signal below 307 nm as a result of the increasing ozone absorption in the Huggins band, the channel 1 diode array is divided into two virtual bands, 1A and 1B, which can be programmed to different integration times in order to optimize the signal-to-noise ratio. For channel 1A an integration time (IT) of 12 s was selected, while channel 1B has an IT of 1.5 s as do the remaining channels. Initially the integration time for channels 1B to 4 was limited to 0.375 s to avoid saturation effects. After a successful uplink of a co-adding software patch in March 1996, GOME achieved its intended 1.5-s integration time, which is required to obtain global coverage.

Once a day (every 14th orbit) GOME solar irradiance measurements are performed when the *ERS-2* satellite crosses the terminator in the north polar region coming from the night side. Since GOME is not equipped to actively track the sun, viewing of the full solar disk is only possible for a time span of about 50 s. Integration times are 0.75 s for all channels, except for the UV channel, where the integration time is doubled. A mean solar spectrum is then constructed from the series of measurements during the solar viewing period.

Two reflectivity spectra measured by GOME under different cloud conditions are shown in Fig. 2. The most prominent spectral features of trace gases visible in the GOME nadir spectra are the O<sub>3</sub> Huggins (UV) and Chappuis bands (VIS); the O<sub>2</sub> A, B, and  $\gamma$  bands; and

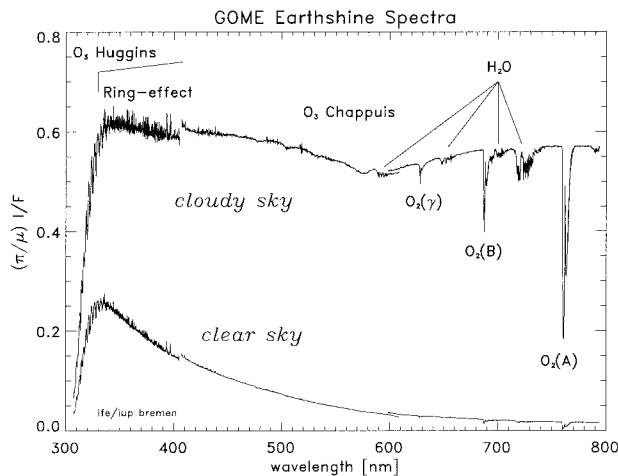


FIG. 2. Sun-normalized earthshine spectra or spectral reflectivity. The two spectra were recorded in September 1995 over the North Atlantic Ocean. Here,  $I$  denotes the earthshine radiance,  $F$  the solar irradiance, and  $\mu$  the cosine of the solar zenith angle. The fractional cloud cover as determined from the  $O_2$  (A) band absorption was zero for the clear-sky scene and one for the cloud scene (see appendix B).

$H_2O$ . Weak absorbers with absorption of less than  $10^{-2}$  are not visible in Fig. 2, but GOME has sufficient signal-to-noise ratio to detect them using the DOAS retrieval (see section 5).

In addition to the four spectral channels, three fast broadband Si diodes with bandwidths approximating the spectral range of channels 2, 3, and 4 are read out every 93.75 ms, such that for each across-track scanning (forward scan) 48 PMD readings are available, each with a subpixel coverage of  $40 \times 20 \text{ km}^2$  on the surface. The relatively high spatial resolution of the PMDs can be also employed for cloud detection as demonstrated in the PMD image shown in Fig. 3, where the three PMD values were assigned to the three basic colors blue (PMD1), green (PMD2), and red (PMD3) to form a true color RGB (red–green–blue) image.

At selected times during the year, normally limited to the second half of the year, a lunar observation sequence is introduced (Dobber et al. 1998). In this measurement mode the scan mirror picks up the moonlight via the nadir view port using a scan mirror angle of  $70^\circ$ – $85^\circ$  from the nadir. On the night side of the orbit GOME performs various regular calibration measurements, such as LED and dark signal measurements. Once a month a detailed wavelength calibration using the onboard calibration lamp is carried out over several orbits. The variation of  $\pm 0.5 \text{ K}$  in the predisperser prism temperature during one orbit causes small shifts in the wavelength axis. The calibration sequence, therefore, permits a temperature-dependent wavelength calibration in each of the four spectral channels by fitting a fourth-order polynomial to selected wavelengths of the measured lamp lines. For each predisperser temperature

measured in steps of  $0.1^\circ \text{ K}$  a set of polynomial coefficients is determined.

The main characteristics of the GOME instrument and its operational modes are summarized in Table 1. Additional details on the GOME operation can be found elsewhere (ESA 1995).

### 3. GOME operational data products

Retrieval of geophysical information from the GOME raw measurements can be divided into two separate steps: the conversion of the raw data (level 0 data) into radiometrically calibrated and geolocated spectra (level 0 to 1 processing), and retrieval of geophysical parameters, such as total columns of ozone and  $NO_2$ , from the calibrated spectra (level 1 to 2 processing). The ground segment of the GOME Data Processor (GDP), which comprises the level 0 to 1 and level 1 to 2 processing, is located at DFD of the DLR, which is part of the official ESA Data Processing and Archiving Facility D-PAF of GOME. The algorithm development of the GDP was led by a group of international scientists from several European and U.S. institutions and experts from ESA and DLR. Only a general overview of the GDP shall be given here. For further details the reader is referred to the DLR and ESA documentations (DLR 1996a,b; ESA 1996).

#### a. Level 0 to 1 data processing (spectral calibration)

Level 0 to 1 processing can be divided into the wavelength calibration (see section 2b) and the radiometric calibration. The radiometric calibration comprises several steps: (i) adjustments of the raw data to account for leakage current, straylight, focal plane assembly (FPA) noise (which is related to the voltage controlling the Peltier coolers), and the detector pixel-to-pixel variability (using onboard LED measurements); (ii) a polarization correction; and (iii) absolute radiometric calibration. The polarization correction is necessary since the instrument optics are polarization sensitive and the backscattered and reflected light from the earth's atmosphere is, in general, partially polarized. The purpose of the polarization correction is to transform the measured signal into an unpolarized signal by taking into account the polarization sensitivity of the instrument known from preflight calibration measurements. The algorithm makes use of the spectral channels, the PMD data, and the instrument polarization sensitivity. In addition, the polarization below 300 nm, for which no PMD information exists, is calculated from Rayleigh single scattering theory. Using this information a wavelength-dependent polarization correction factor can be derived (DLR 1996a, 26–41). Finally, the unpolarized signal units of counts per second are converted into absolute radiometric (earthshine) radiance and (solar) irradiance units.

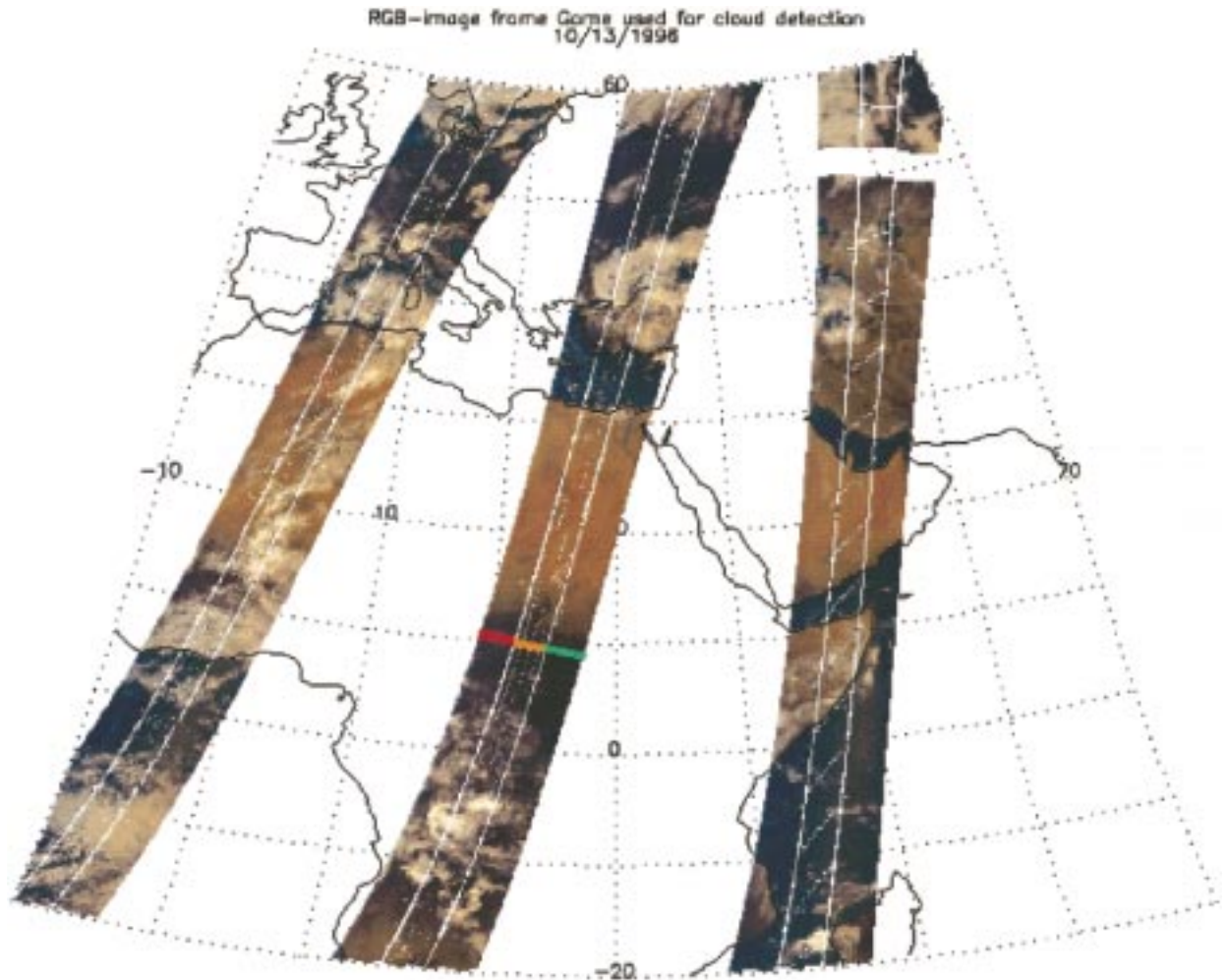


FIG. 3. RGB image of North Africa and Europe produced from the PMD measurements. The three PMDs with broadband coverage of GOME channels 2 (blue), 3 (green), and 4 (red), respectively, are color mixed to obtain this image. One across-track swath of GOME with the west, nadir, and east ground pixels (forward scan) each covering a surface area of  $40 \times 320 \text{ km}^2$  and color-coded in red, yellow, and green is shown in the center orbit. For each ground pixel 16 PMD readings having a surface pixel resolution of  $40 \times 20 \text{ km}^2$  are recorded. The spatial resolution of the PMDs is sufficient to recognize the Nile River bed.

#### b. Level 1 to 2 processing (DOAS retrieval)

The second part of the GDP consists of four parts: (i) DOAS fitting, which derives a total slant column of the selected trace gas in a predefined spectral window, for example, ozone and  $\text{NO}_2$ ; (ii) determination of the cloud cover fraction using the initial cloud fitting algorithm (ICFA), which is necessary in order to account for the trace gas column below the cloud; (iii) calculation of air mass factors (AMFs) for conversion of the slant columns into vertical columns; and (iv) the vertical column density calculation using the results from the preceding steps (DLR 1996b).

The DOAS algorithm determines a slant column amount by least squares fitting a linear combination of reference absorption cross-section spectra of trace gases and a Ring reference spectrum to the measured optical density, that is,

$$\begin{aligned} \tau(\lambda, s) &= -\ln \frac{I(\lambda, s)}{F(\lambda)} \\ &\approx \sum_i \sigma_i(\lambda) \cdot \text{SCD}_i(s) + \sigma_{\text{Ring}}(\lambda) \cdot \text{SCD}_{\text{Ring}}(s) \\ &\quad - \sum_{k=0}^n a_k \lambda^k, \end{aligned} \quad (1)$$

where  $\tau(\lambda, s)$  is the measured slant optical density,  $I(\lambda, s)$  and  $F(\lambda)$  the earthshine radiance and the solar irradiance respectively,  $\sigma_i(\lambda)$  the differential absorption cross section of the  $i$ th molecule at wavelength  $\lambda$ , and  $\text{SCD}_i = \int_s \rho_i(s) ds$  is the integrated number density along the slant optical path  $s$ , which is mainly defined by the solar zenith angle and the viewing geometry of the instrument (line of sight). The unit of SCD is in units of molecule  $(\text{mol}) \text{ cm}^{-2}$ . A basic assumption made in the

DOAS retrieval is that the differential cross section in Eq. (1) is not altitude (temperature) dependent. Even though the cross sections of ozone and nitrogen are temperature dependent, it generally suffices to take the temperature at the number density maximum of the climatological profile to determine the effective cross section.

The Ring effect, which causes the filling-in of solar Fraunhofer lines observed in the backscattered radiation due to inelastic Raman scattering by  $N_2$  and  $O_2$  molecules (Grainger and Ring 1962; Joiner et al. 1995; Vountas et al. 1998), must be accounted for in the slant column retrieval from UV/visible spectra and is treated here as an effective absorber. The Ring reference spectrum can be measured using the cross-polarizer method (Solomon et al. 1987), which was done during the preflight calibration using the GOME spectrometer, or it can be calculated by radiative transfer calculation (Vountas et al. 1998). Reference cross-section spectra for ozone and  $NO_2$  have also been measured with the GOME spectrometer during the preflight calibration (Burrows et al. 1998a,b) and are used along with the GOME Ring reference spectra in the operational retrieval.

A polynomial is subtracted from the measured optical depth in Eq. (1) to remove the broadband spectral structure resulting from Rayleigh and Mie (aerosol) scattering and the slowly varying component of the molecular absorption. Normally, a linear least squares regression to Eq. (1) with the slant column densities  $SCD_i$ ,  $SCD_{Ring}$ , and the regression coefficients  $a_k$  as fitting parameters is carried out. However, in order to improve the relative spectral alignment of the radiance and irradiance as well as the molecular and Ring reference spectra, small shifts and squeezes are performed for each spectrum in addition to the slant column fits, which requires the application of a nonlinear least squares method, in this case the Marquardt–Levenberg method. The spectral windows 325–335 nm (channel 2) and 425–450 nm (channel 3) of GOME have been selected for the operational ozone and  $NO_2$  slant column retrieval, respectively. For other trace gases (see also section 5) appropriate spectral windows are summarized in Table 2.

The conversion of the slant column density into a vertical column density or total column including a correction for clouds is done as follows:

$$VCD_i = \frac{SCD_i + f \cdot GVC_i \cdot AMF_{cld,i}}{fAMF_{cld,i} + (1 - f)AMF_{clr,i}}. \quad (2)$$

Here  $AMF_{clr,i}$  and  $AMF_{cld,i}$  are calculated airmass factors for clear-sky and overcast cloud cover condition;  $f$  is the fractional cloud cover as determined by the observed oxygen A band absorption near 760 nm using the ICFA algorithm (see appendix B); and  $GVC_i$ , the vertical column below the cloud top (*ghost vertical column*), which is not seen by GOME and which is determined by integrating a climatological trace gas profile from the

TABLE 2. DOAS total column retrieval from GOME. S: stratosphere, T: troposphere, cld: cloud correction, and Ring: Ring reference spectra.

Trace gas	Window (nm)	Other fit parameters	Observations
Level 2 products			
$O_3$	325–335	Ring, cld	S: global, T: smog
$NO_2$	425–450	$O_3$ , Ring, cld, smoothing	S: global, T: combustion, biomass burning
Research products			
OCIO	357–381	$NO_2$ , $O_4$ , Ring	S: twilight, polar vortex
BrO	345–359	$O_3$ , $NO_2$ , $O_4$ Ring	T: local, S: polar vortex
$SO_2$	314–327	$O_3$ , Ring	T: volcano
$H_2CO$	337–356	$O_3$ , $NO_2$ , Ring	T: biomass burning
Other candidates			
ClO, $NO_3$ , IO, OBrO, $H_2O_r$			

ground to the cloud-top pressure. Currently, the cloud-top pressure is derived from the International Satellite Cloud Climatology (ISCCP) database (Rossow and Schiffer 1991). In clear-sky condition, that is,  $f = 0$ , Eq. (2) reduces to the more familiar form

$$VCD_i = \frac{SCD_i}{AMF_{clr,i}}, \quad (3)$$

and in the limit  $f = 1$  (complete cloud cover) to

$$VCD_i = \frac{SCD_i}{AMF_{cld,i}} + GVC_i. \quad (4)$$

The airmass factor is defined as the ratio of the slant to the vertical optical density:

$$AMF_i = \tau_{i,s}(\lambda)/\tau_{i,z}(\lambda), \quad (5)$$

which is calculated using the multiple scattering radiative transfer model (RTM) GOMETRAN (Rozanov et al. 1997, 1998), once for an atmosphere with an optical thick cloud acting as a bidirectional reflecting surface and, second, for a cloud-free scenario with a constant surface albedo. The slant optical density (SOD)  $\tau_{i,s}(\lambda)$  is calculated from RTM calculations. The SOD for the specific trace gas is determined by subtracting the logarithm of the backscattered sun-normalized radiance [ $R(\lambda, s) = I/F$ ] including all absorbers from that calculated with the  $i$ th absorber removed [ $R_i(\lambda, s)$ ], that is,

$$\tau_{i,s}(\lambda) = \ln R_i(\lambda, s) - \ln R(\lambda, s) = \ln \frac{R_i(\lambda, s)}{R(\lambda, s)}. \quad (6)$$

The vertical optical density is the vertically integrated climatological number density profile  $\rho_i(z)$  and is given by

$$\tau_{i,z}(\lambda) = \int_z \sigma_i(z, \lambda) \rho_i(z) dz, \quad (7)$$

where  $\sigma_i(z, \lambda)$  is the absorption cross section as a function of altitude  $z$ . In order to derive the airmass factors, the trace gas vertical profile has to be known a priori. In the current version GDP 2.3 the climatological trace gas database from the Max Planck Institute (MPI) for Chemistry 2D model (ozone) and the *U.S. Standard Atmosphere* (nitrogen dioxide) is used. To speed up data processing the airmass factors are calculated in single scattering with a multiple scattering correction derived from a precomputed table. The airmass factors are determined for the center wavelength of the spectral fitting window and are averaged for three line-of-sight angles (minimum, center, maximum) for each ground pixel covered by GOME.

The DOAS approximation requires that the wavelength dependence of the airmass factor in the spectral fitting window can be neglected, which is the case for weak absorbers. However, ozone in the UV spectral range 325–335 nm cannot be considered a weak absorber and the airmass factor spectrum shows a rather significant wavelength dependence. In appendix C it is shown that a DOAS retrieval of total ozone in the Huggins band is still possible, by calculating the airmass factor at the wavelength, where the ozone absorption is largest, here at 325 nm. An alternative approach is the derivation of ozone columns from the Chappuis band in the visible range, where the ozone absorption is weaker. The Chappuis band retrieval of ozone has been demonstrated to work well (Eisinger et al. 1996a) but is not yet operationally implemented.

### c. Validation of GOME data products

After the initial instrument performance tests, the first GOME data products were made available to the validation campaign participants in July 1995. The major activities of the GOME commissioning phase, which took place from July 1995 up to June 1996, were the checking and the validation of the radiometric accuracy of spectral radiances and irradiances (level 1 products), the comparison of total ozone and  $\text{NO}_2$  with collocated ground-based measurements, and the optimization of the trace gas retrieval. Based on the GOME Validation Campaign Final Results Workshop held on 24–26 January 1996 (ESA 1996), a first set of recommendations concerning further improvements of the quality of the GOME data products were reported and later implemented. A full account of the validation activity is beyond the scope of this paper; however, some of the more relevant issues shall be discussed here.

*Irradiance monitoring.* Initial comparison of the solar irradiance with measurements from the SOLSPEC mission (Thuillier et al. 1997) indicated some changes in the instrument response function, which were associated with changes in the vacuum condition in orbit to that on the ground during the preflight calibration. An improvement in correcting the preflight response function was achieved by reanalyzing the onground thermal vac-

uum measurements and by combining these results with line intensity ratios measured in flight with the internal spectral line lamp (Hoekstra et al. 1996). A periodic update of the in-flight calibration, which also accounts for long-term degradation effects resulting from extended exposure to the radiation in space, is planned to be provided regularly in the near future. For the trace gas retrieval using the DOAS approach the instrumental effects are not critical since these changes are generally broadband and are removed from the differential absorption spectrum by subtracting a fitted polynomial.

*Total ozone validation.* The retrieval accuracy of the ozone slant column densities are on the order of 1%. The additional uncertainty for the vertical column stemming from the AMF calculation, where an a priori profile has to be assumed, is difficult to assess and is conservatively estimated to be 5% for solar zenith angle (SZA) less than  $70^\circ$ . Extensive comparisons between GOME total ozone with the monitoring network of ground-based Dobson, Brewer, SAOZ, and DOAS zenith sky measurements have been made. After some modification, for instance, improving the GDP airmass calculation by selecting a more representative wavelength (325 nm) in the ozone spectral window (325–335 nm) as described in appendix C and by extending the multiple scattering correction up to an SZA of  $90^\circ$ , an agreement of better than  $\pm 4\%$  between GOME retrieved ozone and the ground-based measurements at mid-European stations was found (Lambert et al. 1997; Ladstätter-Weissenmayer et al. 1996; Eisinger et al. 1996a). A direct comparison between GOME total ozone measured above Bremen ( $53^\circ\text{N}$ ,  $9^\circ\text{E}$ ) with ground-based DOAS measurements with a zenith sky viewing visible spectrometer is shown in Fig. 4. No systematic differences between the Bremen ground-based observation and the GOME measurements are observed. Further details on recent comparisons between GOME and other space sensors and a large ground-based network with pole-to-pole coverage can be found elsewhere (Lambert et al. 1999).

*$\text{NO}_2$  total column validation.* From the DOAS retrieval the accuracy of the slant columns is on the order of 12%–15% for solar zenith angles above  $40^\circ$  (midlatitudes and up) and increases to 25% below  $20^\circ$  (Tropics). In cases of very low stratospheric  $\text{NO}_2$  amounts the errors can become even larger at low solar zenith angles (detection limit at about  $2 \times 10^{15}$  mol  $\text{cm}^{-2}$  slant column density, here defined as the 100% retrieval error limit). The validation of the  $\text{NO}_2$  total column is still at a preliminary stage because (i) the number of ground-based stations measuring  $\text{NO}_2$  is small compared to the well-established global networks of stations measuring ozone and (ii) the significant and variable amount of tropospheric nitrogen dioxide is usually not detected in most ground-based zenith-sky measurements, which focus on monitoring the stratospheric amount. Indeed, the GOME  $\text{NO}_2$  total columns tend to be significantly higher than the ground-based values and the difference ob-

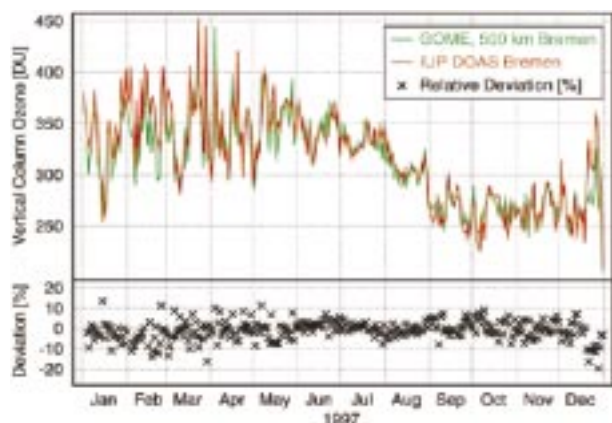


FIG. 4. Validation of GOME total ozone above Bremen ( $53^{\circ}\text{N}$ ,  $9^{\circ}\text{E}$ ) in 1997. Daily total ozone means of all measurements by GOME within a 500-km radius around Bremen (green) and daily means from a series of morning and evening measurements obtained using a zenith-sky viewing spectrometer located at the University of Bremen, Germany (red), are shown at the top. The relative deviation between GOME and ground-based DOAS in percent is shown at the bottom. Most of the larger deviations are observed during winter/spring, where the natural total ozone variability is largest. Differences in viewing geometries and the local time between space-borne and ground-based measurements also significantly contribute to the largest deviations observed.

served is best explained as resulting from the tropospheric amount detected by GOME. However, the  $\text{NO}_2$  AMFs depend on the vertical profile selected to be used in the radiative transfer calculation, and the sensitivity of the  $\text{NO}_2$  AMF with respect to the tropospheric column seems to lead to an overestimation of the derived total column particularly in cases of low surface albedos. This explains why the global  $\text{NO}_2$  columns derived from GOME are still declared intermediate results subject to further modification. Global distribution of nitrogen dioxide measured by GOME still provides valuable information on the variability of  $\text{NO}_2$ , which is strongly dependent on its tropospheric loading (see section 4).

#### 4. GOME observation of $\text{O}_3$ and $\text{NO}_2$

Observations of the Antarctic ozone hole in October using GOME data in the years 1995–97 are shown as monthly mean values in Fig. 5. From this series it can be seen that the ozone hole, here arbitrarily defined as the region with less than 220 DU total ozone, extended to an area of about  $20 \times 10^6 \text{ km}^2$  in each of the three years, which is nearly the size of the North American continent. The geographic extent of the Antarctic ozone hole, however, has not significantly increased due to the limited area of the polar vortex, a cyclonic wind system, which starts to form during polar night. Minimum average values of less than 150 DU have been observed in each of the last three years by GOME during October. Two conditions have to be met in order to have rapid catalytic destruction of ozone (WMO 1995; EC 1997). First, stratospheric temperatures have to be sufficiently

cold for formation of polar stratospheric cloud (PSC). On the surface of the PSCs heterogeneous reactions on the PSC surface convert inactive chlorine compounds, particularly chlorine nitrate and  $\text{HCl}$ , into more photochemically active forms, such as  $\text{Cl}_2$ . Such conditions usually prevail inside the polar vortex. Second, after sunlight enters the polar region during spring,  $\text{Cl}_2$  is rapidly photolyzed into active  $\text{ClO}_x$  species involved in the rapid catalytic ozone destruction cycle.

Despite the fact that Northern Hemispheric (NH) stratospheric temperatures are generally warmer than in the Antarctic, a similar but weaker development of an ozone hole is expected to occur in the Arctic spring. The March mean total ozone from the years 1996–98 are depicted on the left-hand side of Fig. 5. An NH ozone hole was observed in 1996 and 1997, where minimum values slightly above 300 DU on average were observed, about 150 DU less than the observed ozone winter/spring maximum outside the vortex. Less frequent PSC formation than in the previous cold winters (Naujokat and Pawson 1996) was observed during the winter 1997/98 (B. Naujokat 1998, personal communication) and less significant NH ozone depletion was observed in March 1998. The sequence of GOME observations clearly demonstrates the high year-to-year variability of total ozone currently observed in the NH winter/spring. In March 1996 and 1998 the lowest ozone was measured on the European and Atlantic side of the polar region. This is indicative of air mass exchanges between subtropical (ozone poor air, cold stratospheric temperatures) and midlatitude regions (ozone rich air, warm temperatures) and the polar region, which occur mainly in northern Europe and the North Atlantic. These processes can lead to either dynamical ozone losses (minihole events) or to sudden increases in ozone levels, respectively. Despite the strong dynamic variability of ozone in the NH, enhanced levels of  $\text{ClO}_x$  have been observed in some of the Arctic winters (Santee et al. 1996, 1997) and chemical ozone losses have been shown to contribute significantly to the ozone reduction observed in the winters 1995/96 and 1996/97 (Müller et al. 1997a,b; Rex et al. 1997). The global annual total ozone climatology in Fig. 6 clearly shows the similarity between the spring ozone hole observed by GOME in the SH and NH, despite the hemispheric differences in the overall total ozone levels.

Figure 7 shows a 1-day composite of total ozone and nitrogen dioxide distribution in the NH observed on 1 April 1997. Inside the polar vortex, whose edges are indicated by the black contour lines of potential vorticity, both ozone and  $\text{NO}_2$  total columns were significantly reduced. Several explanations for the reaction mechanism responsible for the low  $\text{NO}_2$  inside the vortex are possible, of which (i) the heterogeneous reaction  $\text{N}_2\text{O}_5(\text{g}) + \text{H}_2\text{O}(\text{s}) \rightarrow 2\text{HNO}_3(\text{s})$ , removing the nighttime reservoir of  $\text{NO}_2$ ; (ii) the gas phase chemistry through the reaction  $\text{NO}_2 + \text{OH} + M \rightarrow \text{HNO}_3 + M$ , requiring low temperatures and sunlight to produce suf-

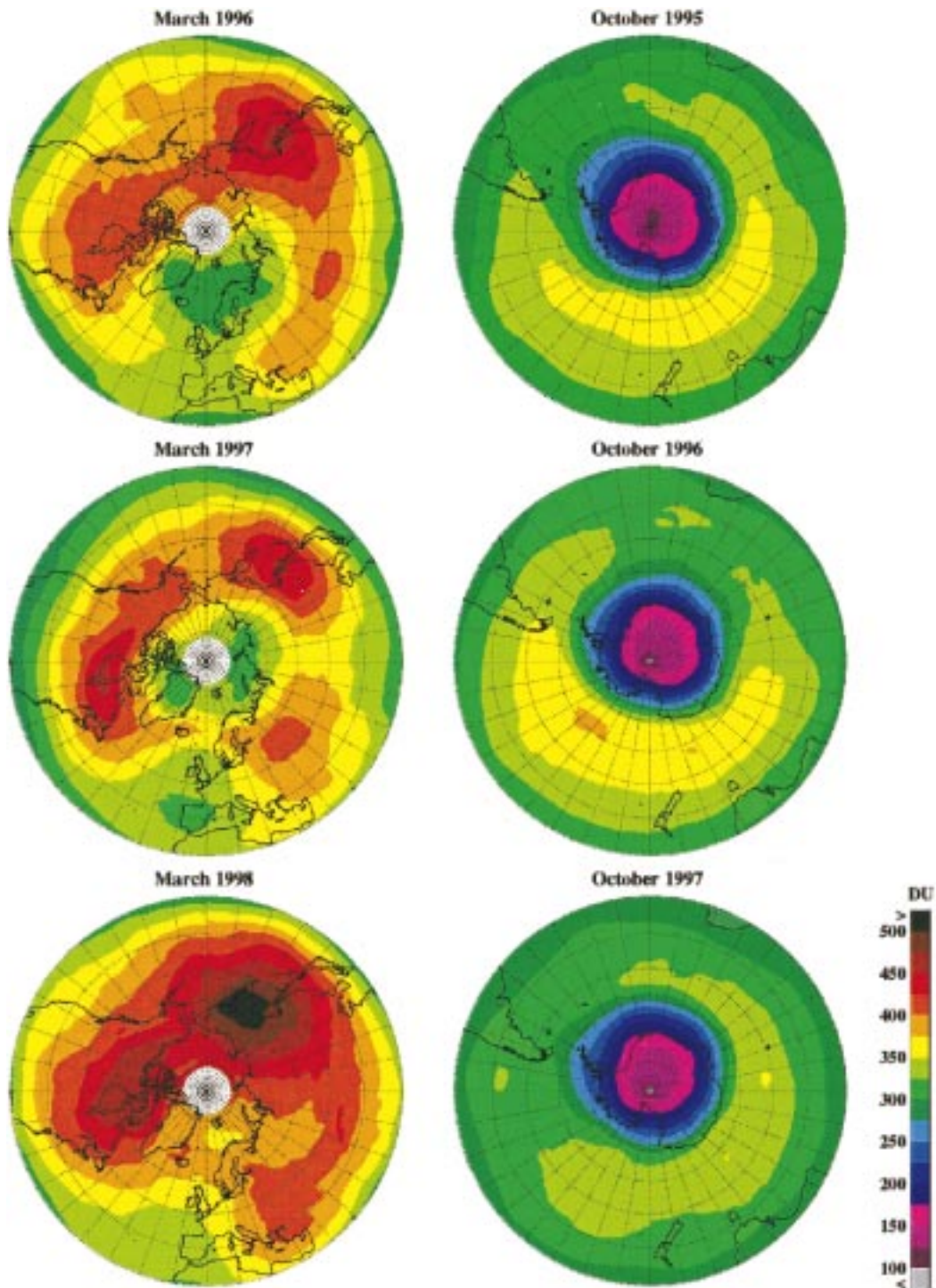


FIG. 5. Northern and Southern Hemispheric monthly mean total ozone measured by GOME in March 1996–98 (left, top to bottom, Arctic) and October 1995–97 (right, top to bottom, Antarctica). The means were calculated from the GDP level 2 version 2.0 data, except for 1995 and 1998, which were calculated from the version level 2.3 data. The difference between version 2.0 and 3.0 is less than 3%.

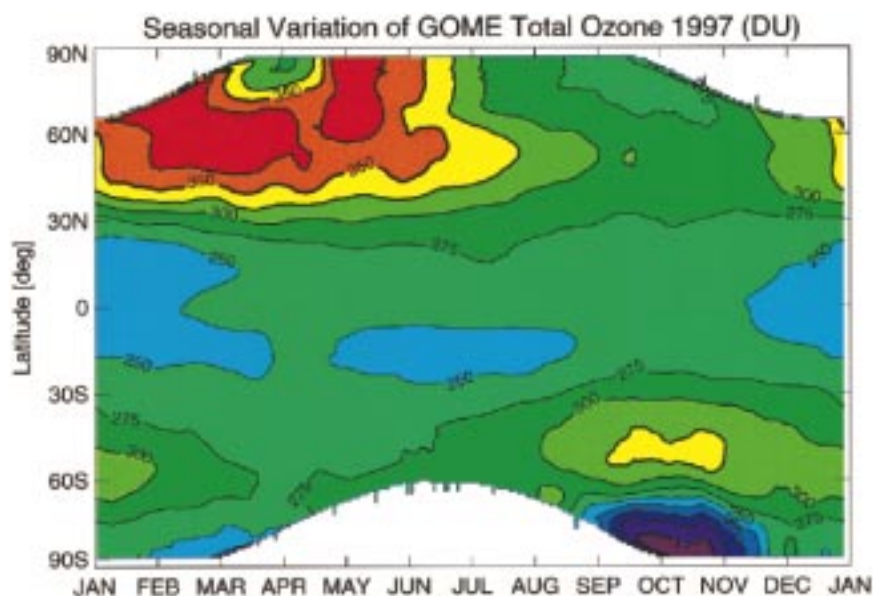


FIG. 6. Annual GOME total ozone climatology from 1997. For the blank areas no GOME measurements are available because it is polar night.

ficient amounts of OH radicals; and (iii) formation of less  $N_2O_5$  at night due to low ozone in combination with the slowed  $N_2O_5$  photolysis during the day because of the low temperatures inside the vortex may be considered the most relevant ones (Lary et al. 1994; Solomon and Garcia 1983; Noxon 1979). PSC formations in 1997 were still possible until late March, where record minimum temperatures have been observed (Coy et al. 1997). It is therefore possible that after denitrification (sedimentation of  $HNO_3$  by reaction (i) the  $NO_x$  released by the photolysis of  $HNO_3$  is not in excess compared to the total  $ClO_x$ . This means that  $NO_2$  is still converted back into chlorine nitrate, which can last several weeks beyond the last possible PSC occurrence.

As GOME regularly crosses the polar regions in its sun-synchronous orbit, GOME observations at different daytimes are possible at high latitudes. The  $NO_2$  diurnal variation observed inside the late polar vortex in early April 1997 is very small as compared to a later period where the observations were made at the same location, but outside the polar vortex (Fig. 8). The reduced diurnal variation inside the vortex speaks in favor of the aforementioned reaction schemes (i) and (iii) and can be also interpreted as a consequence of prolonged denitrification.

It should be noted that enhanced tropospheric emission of  $NO_2$  arising most likely from urban pollution is observed in the northeast of the United States and part of Europe on 1 April 1997 (see Fig. 7). This demonstrates the capability of GOME of detecting tropospheric and stratospheric  $NO_2$ .

## 5. New research from GOME

A large and growing scientific user community is working on new research products, which exploit the

full spectral information available from GOME. Selected highlights on the retrieval of minor trace gases, using as an example OCIO, a stratospheric constituent observed under ozone hole conditions over Antarctica, and tropospheric BrO, measured during polar spring and early summer are presented in sections 5a and 5b. Regional events, such as sulphur dioxide emission from the eruption of the Nyamuragira volcano in December 1996 (section 5c) and tropospheric pollution during the Indonesian forest burning in summer 1997 (section 5d) are good examples of the capability of GOME to detect minor trace gases in the troposphere. GOME spectra showing the differential absorption of  $SO_2$ , OCIO, and BrO and the corresponding wavelength ranges used to derive the slant column densities are depicted in Fig. 9. Table 2 summarizes the various trace constituents, which have been successfully retrieved by DOAS from GOME observations, and their geographical distribution. Several other species, for instance ClO and  $NO_3$ , which have absorption in the GOME spectral range, have not yet been investigated but are potential candidates for future studies.

### a. OCIO over Antarctica in 1995

Chlorine dioxide (OCIO) links the BrO and ClO catalytic ozone destruction cycles known to contribute to the observed stratospheric ozone losses during polar winter/spring. The only established source of stratospheric OCIO is the reaction between BrO and ClO (McElroy et al. 1986). OCIO shows a strong diurnal variation because it is rapidly photolyzed during the day. It is, therefore, expected that OCIO can be primarily detected at high solar zenith angles. Slant columns of

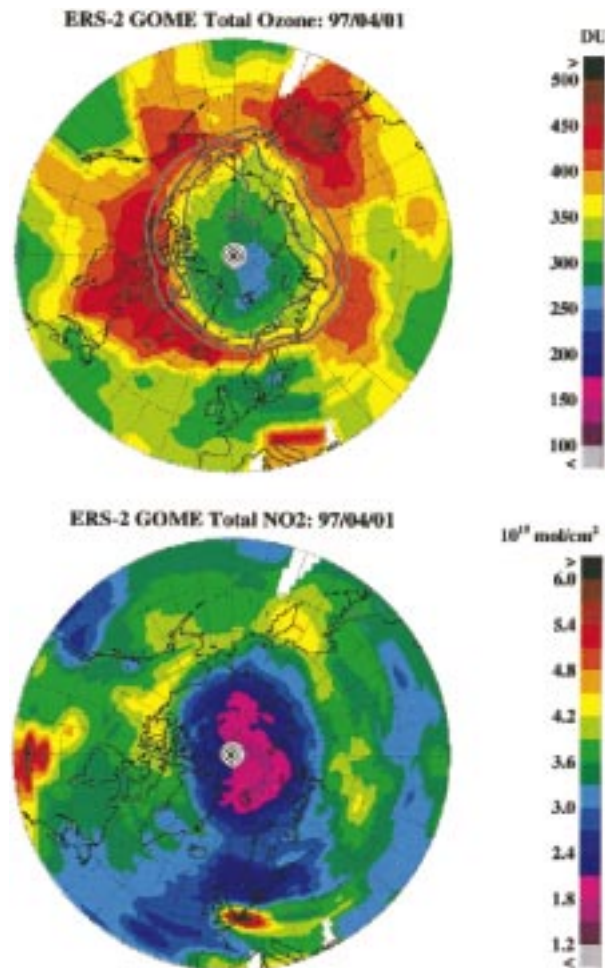


FIG. 7. Total  $O_3$  (top) and  $NO_2$  (bottom) measurements in the Arctic from 1 April 1997. Solid lines indicate the approximate edge of the polar vortex (potential vorticity  $36, 42, 48 \times 10^{-6} \text{ K m}^2 \text{ kg}^{-1} \text{ s}^{-1}$  at 475 K from the European Centre for Medium-Range Weather Forecasts analysis).

OCIO determined as a function of solar zenith angle during the Antarctic spring 1995 are shown in Fig. 10. Since for SZA between  $86^\circ$  and  $94^\circ$  the AMF remains nearly constant, it can be concluded that the vertical column also increases with SZA. This SZA dependence of the column amount is a measure of the diurnal variation of OCIO related to its rapid photolysis. Similarly, the higher the solar zenith angle, the closer the chlorine dioxide measurements move toward the polar vortex center, where enhanced local OCIO production may occur. Between July and mid-September enhanced OCIO diurnal variation can be observed, while later starting in October the OCIO levels fall off near or below the detection limit, estimated to be  $1 \times 10^{14} \text{ mol cm}^{-2}$  in the slant column or  $1 \times 10^{13} \text{ mol cm}^{-2}$  in the vertical column density. This seasonal behavior is in excellent agreement with observations made at McMurdo Station ( $78^\circ\text{S}$ ) (Sanders et al. 1993). At low  $ClO_x$  background levels, OCIO correlates well with ClO; however, above

a certain threshold OCIO becomes a rather poor indicator of the ClO levels (Sessler et al. 1995). Nevertheless, the measurements presented support the indicator role of OCIO distinguishing between low (background) and medium/high (disturbed) ClO cases, switching to high levels once ClO concentrations exceed a certain threshold.

#### b. Arctic tropospheric BrO during spring/summer

The role of the BrO radical in stratospheric chemistry and catalytic ozone depletion in particular has been recognized for some time. More recently it became clear that under certain conditions BrO can also act as a catalyst of tropospheric ozone destruction (Le Bras and Platt 1995). This is thought to be the main reason for periods of strongly reduced tropospheric ozone levels (*tropospheric low ozone events*), which have been observed in the Antarctic and Arctic during spring. During such events enhanced concentrations of filterable bromine (Barrie et al. 1988) and BrO (Hausmann and Platt 1994) have been detected, and some evidence of enhanced ClO concentrations has also been found.

The first studies of GOME BrO columns were mainly concerned with stratospheric BrO (Eisinger et al. 1996b, Hegels et al. 1998) and showed the potential of global BrO detection by the instrument. Wagner and Platt (1998) found the first evidence of tropospheric BrO signals in the GOME measurements. They analyzed a large plume of BrO over Antarctica, and by comparing the retrieved amounts of BrO with the total  $Br_y$  content of the stratosphere they concluded that for this cloud-free situation the BrO had to be located in the troposphere. The study of Richter et al. (1998) has focused on the Northern Hemisphere and showed that enhanced tropospheric BrO columns were common events in Arctic regions during spring and early summer 1997.

Ground-based measurements of tropospheric BrO in remote regions are restricted to a few stations. In contrast the GOME measurements offer a global view and an example is given in Fig. 11, where total BrO columns are shown for three days in April 1997. In the Hudson Bay area and parts of the Canadian Arctic enhanced columns indicate a large tropospheric BrO cloud. In this region enhanced BrO values were detected on many days from February to May 1997, which indicates a large and continuous local source of BrO. Enhanced BrO values are also seen along the coastlines of the Arctic Sea and toward the pole, in agreement with ground-based measurements in these areas. These results further confirm the model of bromine release from sea salt via activation on pack ice. After June no further BrO events were detected by GOME in the Northern Hemisphere, showing that bromine activation in polar regions is in fact restricted to the spring season, when ice is present.

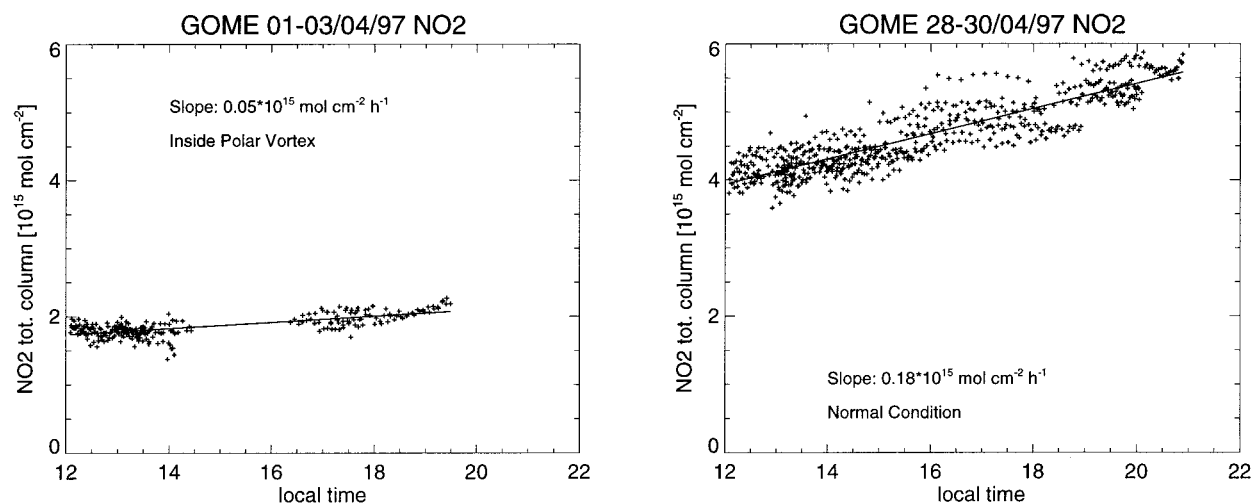


FIG. 8. Diurnal variation of NO<sub>2</sub>. The diurnal variation of NO<sub>2</sub> columns inside the vortex (1–3 April 1997, column growth of  $0.05 \times 10^{15}$  mol cm<sup>-2</sup> h<sup>-1</sup>) and after the vortex breakup (28–30 April 1997, column growth of  $0.18 \times 10^{15}$  mol cm<sup>-2</sup> h<sup>-1</sup>) are shown. All GOME measurements located within a radius of 500 km centered at 80°N, 60°E are included.

### c. Volcanic SO<sub>2</sub>

Sulfur dioxide released from large volcanic eruptions can be injected directly into the lower stratosphere, where it is oxidized to sulfuric acid and combines with water to form stratospheric sulfate aerosols. Heterogeneous reactions on aerosols can affect global ozone chemistry (Jackman et al. 1996) and alter the radiation budget of regional and global climate due to aerosol scattering and absorption. The most prominent volcanic eruptions with global impact within the last two decades were the El Chichon (1982) and Mount Pinatubo (1991) events.

GOME observed SO<sub>2</sub> from an eruption of the Nyamuragira volcano in Zaire, a shield volcano near the border of Rwanda (Eisinger et al. 1997). The eruption started on 1 December 1996 and four days later the plume reached an altitude of 12 km, still well below the tropopause at tropical latitudes. Figure 12 displays SO<sub>2</sub> slant columns derived from the GOME radiances during the 12 days following the first reported eruption. In order to visualize the extent of the volcanic SO<sub>2</sub> plume, 3-day composites giving full surface coverage in the region around the volcano are shown. A rough estimate of the total column amount can be obtained by dividing the measured slant column by a factor of 2.

The maximum SO<sub>2</sub> slant column of 54.7 DU was observed on the first day of eruptions on 1 December 1996. On this day a SO<sub>2</sub> cloud was already observed stretching up to 2000 km westward (10°E) from Nyamuragira, which may be explained by SO<sub>2</sub> emissions preceding the major eruption. High slant columns observed in the following days indicate further outgassing of volcanic SO<sub>2</sub>, either continuously or in several large bursts, which is characteristic of an effusive eruption (as opposed to an explosive eruption) as expected for a rift volcano like Mount Nyamuragira (Krueger et al.

1995). Most of the SO<sub>2</sub> emission was transported to the west, consistent with mean wind directions in Nairobi and Bangui observed in December 1981 at 10-km altitude (Krueger et al. 1996). Adding up all the contribution of SO<sub>2</sub> within a given 3-day period leads to an estimated lower limit of a few hundred kilotons for the December 1996 eruption, which is much lower than the 3 Mt observed by the TOMS in the December 1981 eruption (Krueger et al. 1996).

### d. Indonesian fire and biomass burning

During biomass burning, hydrocarbons are emitted that are oxidized to aldehydes, ketones, organic acids, and other oxygenated hydrocarbons. These trace gases are known to be produced in combustion (Crutzen 1979; Crutzen et al. 1985; Andreae et al. 1988). In the upper troposphere, formaldehyde (H<sub>2</sub>CO) is formed during the oxidation of methane, whereas in polluted regions, it is produced additionally in significant amounts by oxidation of the hydrocarbons emitted from both anthropogenic and biogenic sources. H<sub>2</sub>CO, which is a source of HO<sub>2</sub> radicals in the atmosphere, plays an important role in photochemistry and tropospheric ozone production in the aging plumes resulting from biomass fires. Nitrogen dioxide is also produced by combustion processes (urban pollution) and biomass burning and also contributes to tropospheric ozone production. During biomass burning in summer/fall 1997 over Borneo excess tropospheric columns of NO<sub>2</sub> and ozone and total columns of H<sub>2</sub>CO were observed by GOME (Fig. 13). In the Tropics the background ozone and to a somewhat lesser extent NO<sub>2</sub> vertical distribution show relatively little variation in the absence of regional pollution. It is, therefore, possible to subtract the vertical columns of ozone and NO<sub>2</sub> from a clean air region (e.g., in the

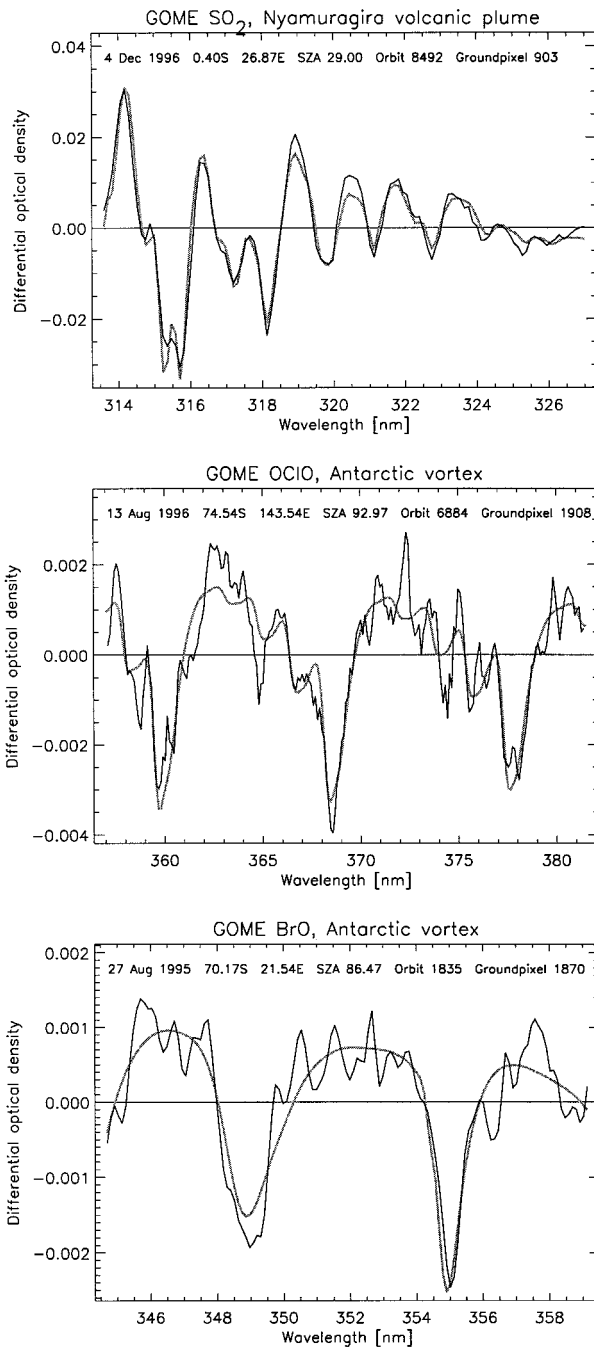


FIG. 9. GOME DOAS fit results (black lines) for SO<sub>2</sub> (top), OClO (middle), and BrO (bottom) (Eisinger et al. 1997). The fit results for specific absorbers are obtained after subtracting all other molecular species fitted in the same spectral window and the polynomial. The scaled reference absorption cross section spectra are shown by the smooth lines. The difference between each fit result and the corresponding reference spectrum is called the fit residual of that molecule.

Pacific) to obtain the *excess vertical columns* of this trace gas stemming from the pollution.

The heavy fires over Borneo (0°, 115°E) lasted from July to September 1997, with some minor burning re-

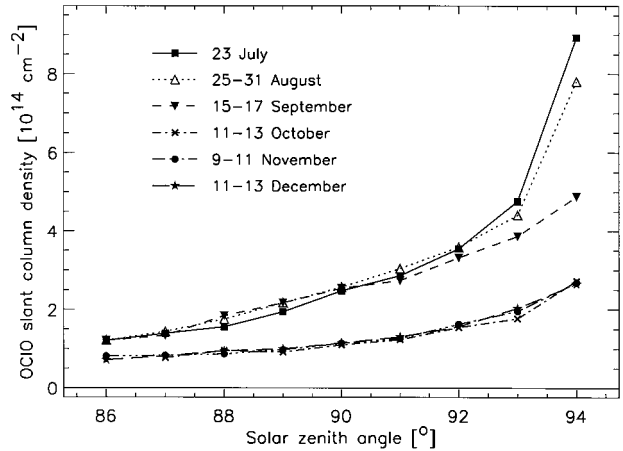


FIG. 10. Antarctic OClO diurnal profiles (Eisinger et al. 1997). The data are from July to December 1995. Each measurement has been binned into 1° steps and averaged. The detection limit for OClO is reached at a slant column of about  $1 \times 10^{14}$  mol cm<sup>-2</sup>.

maining until the end of the year. The heavy monsoon rains normally expected during these months were absent (possibly related to El Niño weather phenomena), which caused the unusual dry condition in this region. Heavy smog condition in the metropolitan areas of Jakarta, Kuala Lumpur, and Singapore also lead to high tropospheric NO<sub>2</sub>, ozone, and formaldehyde in the urban regions. Kuala Lumpur was also lying in the westward wind direction from Borneo. Under normal conditions the concentrations of NO<sub>2</sub> and H<sub>2</sub>CO are low and near or below the detection limit but under polluted conditions the total column amounts of NO<sub>2</sub> were increased from about 0.8 to 2–4 ( $\times 10^{15}$ ) mol cm<sup>-2</sup> (~0.6 ppb) and the tropospheric vertical columns of H<sub>2</sub>CO

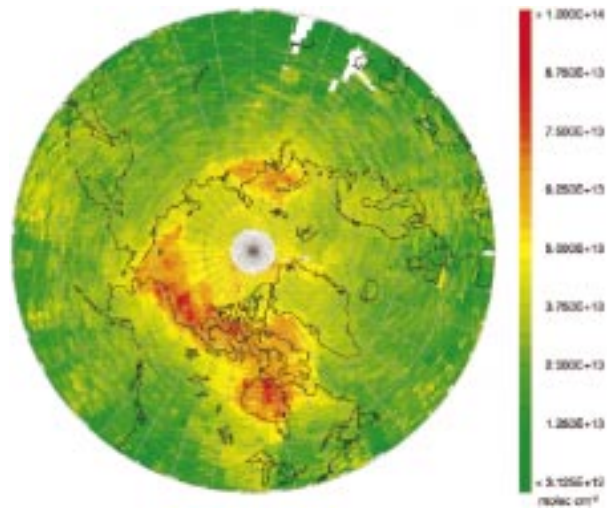


FIG. 11. GOME BrO vertical columns in the Arctic for 14–16 April 1997. The values are in units of mol cm<sup>-2</sup>. The derived BrO columns have been gridded into  $0.25^\circ \times 1^\circ$  bins and averaged over the 3-day period.

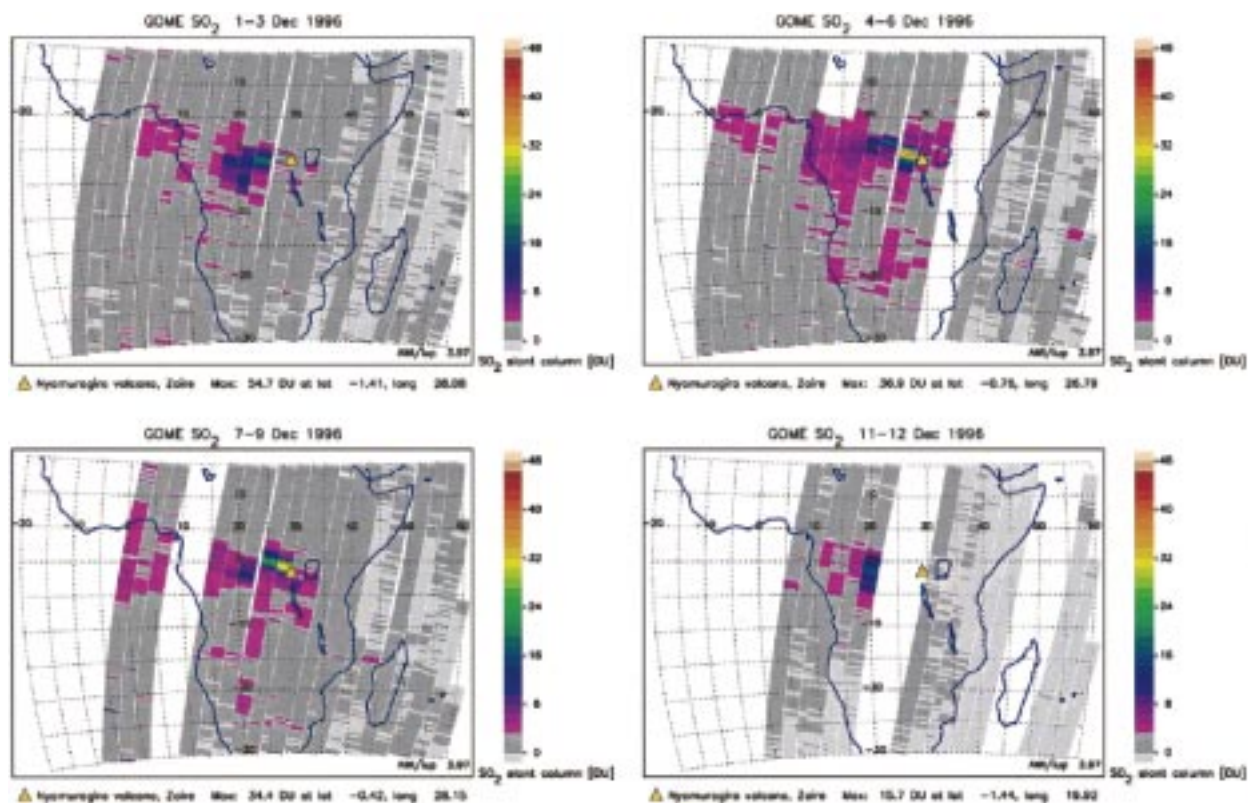


FIG. 12.  $\text{SO}_2$  plume evolution from the Nyamuragira volcanic eruption in Zaire (Eisinger et al. 1997). The eruption started on 1 December 1996 and continued emission of sulfur dioxide are still visible at later periods. For complete surface coverage GOME orbits from three successive days have been combined in each panel.

amounted to up to  $2 \times 10^{16}$  mol  $\text{cm}^{-2}$  ( $\sim 4$  ppb). An excess of 25–30 DU of ozone were reached over Borneo and Sumatra during the period of biomass burning (Fig. 13).

## 6. Vertical ozone profile retrieval

In the wing of the Hartley–Huggins bands of ozone below 320 nm, ozone absorption increases exponentially with decreasing wavelength (see Fig. 2). The combined increase of the scattering height due to Rayleigh scattering and of the ozone absorption at decreasing UV wavelengths provides important information about the ozone column density as a function of height. The use of an inversion scheme to derive height-resolved ozone information from the radiance measured at the top of atmosphere (TOA) using a nadir viewing space instrument has been successfully demonstrated with the series of SBUV (Solar Backscatter UV) and SBUV/2 sensors operating in the UV/visible spectral range (Barthia et al. 1996). A similar backscatter UV technique, called FURM (Full Retrieval Method), has been optimized for the GOME retrieval (de Beek et al. 1997) and is based upon an advanced optimal estimation scheme that includes a priori profiles, for instance, from a climatological database, in order to stabilize the iterative ozone

retrieval (Rodgers 1976, 1990), and an information matrix approach (Kozlov 1983; Hoogen et al. 1998, manuscript submitted to *Phys. Chem. Earth*). The SBUV/2 instruments provide 12 spectral points with a bandwidth of 1.1 nm each between 255 and 340 nm. GOME, on the other hand, provides continuous and extended spectral coverage, therefore providing additional information on aerosols and surface reflectivity, which are simultaneously fitted along with height-resolved ozone concentration.

In the optimal estimation approach the weighted sum of squares between measured and modeled sun-normalized radiances and between the modeled atmospheric and the a priori parameters is minimized by adjusting the atmospheric state vector  $\mathbf{x}_{i+1}$  in iterative steps, as follows:

$$\mathbf{x}_{i+1} = \mathbf{x}_a + (\mathbf{K}_i^T \mathbf{S}_y^{-1} \mathbf{K}_i + \mathbf{S}_a^{-1})^{-1} \times \mathbf{K}_i^T \mathbf{S}_y^{-1} [\mathbf{y} - \mathbf{y}_i + \mathbf{K}_i (\mathbf{x}_i - \mathbf{x}_a)] \quad (8)$$

(Rodgers 1976). Here  $\mathbf{x}_i$  and  $\mathbf{x}_{i+1}$  are the calculated atmospheric state vectors after iterations  $i$  and  $i + 1$ , respectively;  $\mathbf{x}_a$  is the a priori state vector; and  $\mathbf{y}$  and  $\mathbf{y}_i$  the measured sun-normalized and calculated radiances, respectively. Matrices  $\mathbf{S}_y$  and  $\mathbf{S}_a$  are the measurement error covariance and the a priori covariance matrix, re-

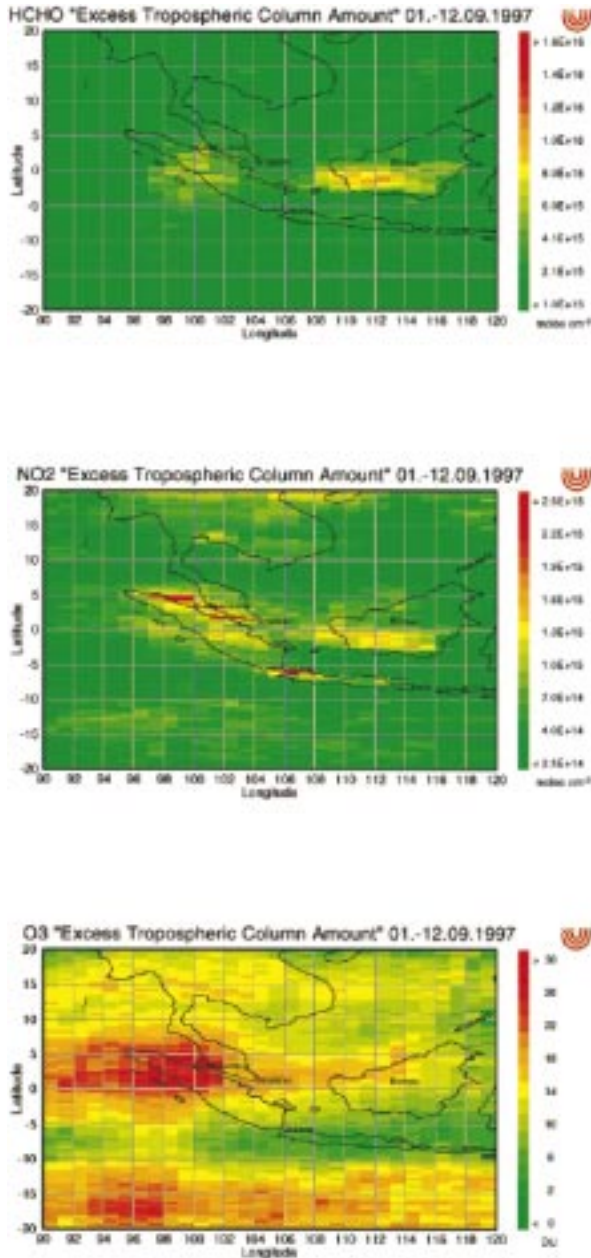


FIG. 13. Tropospheric emission during the Indonesian fires. Twelve-day composites of tropospheric vertical columns ( $\text{mol cm}^{-2}$ ) of  $\text{H}_2\text{CO}$ , excess vertical columns of  $\text{NO}_2$  ( $\text{mol cm}^{-2}$ ), and ozone (DU) determined from GOME measurements during the period between 1 and 12 September 1997 are shown. For the explanation of excess vertical columns see text.

spectively, and  $\mathbf{K}_i$  is the weighting function matrix. The weighting function matrix  $\mathbf{K}_i$  and the radiances  $\mathbf{y}_i$  are determined by RTM calculation using GOMETRAN, where the state vector  $\mathbf{x}_i$  is the model input (Rozanov et al. 1997, 1998). After convergence of the solution vector, the final retrieval error covariance matrix is given by

$$\mathbf{S} = (\mathbf{K}_i^T \mathbf{S}_y^{-1} \mathbf{K}_i + \mathbf{S}_a^{-1})^{-1}, \quad (9)$$

whose diagonal elements are the  $1 \sigma$  variances of the ozone concentration at a given height. Both errors from the noise of the spectral measurements and from the a priori statistics enter the retrieval error calculation. In addition to the ozone profile, scalar parameters such as the aerosol optical thickness, surface albedo,  $\text{NO}_2$  total column, a scaling factor for the pressure profile, an offset for the temperature profile, and the amplitude of the Ring reference spectrum are part of the atmospheric state vector, which are iteratively adjusted. For accurate radiance calculations GOMETRAN solves the multiple scattering RTM equations for 81 equidistant horizontal layers 1 km thick; however, the altitude resolution for the GOME profiles is about 6–8 km in the lower stratosphere and higher above and below. This means that the rank of the weighting function matrix is less than the dimension of the state vector. An elegant way to reduce the number of available fit parameters to that with relevant information content is to develop the difference between  $\mathbf{x}_{i+1}$  and  $\mathbf{x}_a$  into a linear combination of eigenvectors  $\Psi_{i,n}$  of the information matrix  $\mathbf{P}_i$ ; that is,

$$\mathbf{x}_{i+1} - \mathbf{x}_a = \sum_n \beta_{i,n} \Psi_{i,n}, \quad (10)$$

with the eigenvalue equation given by

$$\mathbf{P}_i \Psi_{i,n} = \mathbf{S}_a \mathbf{K}_i^T \mathbf{S}_y^{-1} \mathbf{K}_i \Psi_{i,n} = \Lambda_{i,n} \Psi_{i,n}, \quad (11)$$

where  $\Lambda_{i,n}$  is the  $n$ th eigenvalue of the information matrix. It can be shown that only those eigenvectors with eigenvalues greater than unity contain significant information and need to be retained in the expansion of Eq. (10) (Rodgers 1996). This considerably improves the numerical stability of the retrieval. The information matrix  $\mathbf{P}_i$  is closely related to the information content of the measurement, which can be defined as the reduction in entropy of the possible ensemble of atmospheric states after the measurement with respect to that given by the a priori statistics (Shannon and Weaver 1962). The expansion coefficients  $\beta_{i,n}$  can be obtained by inserting Eqs. (10) and (11) into Eq. (9), that is,

$$\beta_{i,n} = \frac{\Lambda_{i,n}}{N_{i,n}(1 + \Lambda_{i,n})} \Psi_{i,n}^T \mathbf{K}_i^T \mathbf{S}_y^{-1} [\mathbf{y} - \mathbf{y}_i + \mathbf{K}_i(\mathbf{x}_i - \mathbf{x}_a)]. \quad (12)$$

For the derivation of Eq. (12), the biorthogonality relation

$$\langle \Psi_{i,k}^T, (\mathbf{K}_i^T \mathbf{S}_y^{-1} \mathbf{K}_i) \Psi_{i,l} \rangle = \delta_{kl} N_{i,k} \quad (13)$$

has been used (Hoogen et al. 1998, manuscript submitted to *Phys. Chem. Earth*).

For the profile retrieval the GOME spectral range between 290 and 350 nm is used. Similar to the DOAS fit a shift and squeeze of the various spectra (earthshine radiance, solar irradiance, and absorption and Ring reference spectra) are applied to improve the spectral alignment. The new ozone climatology and statistics from

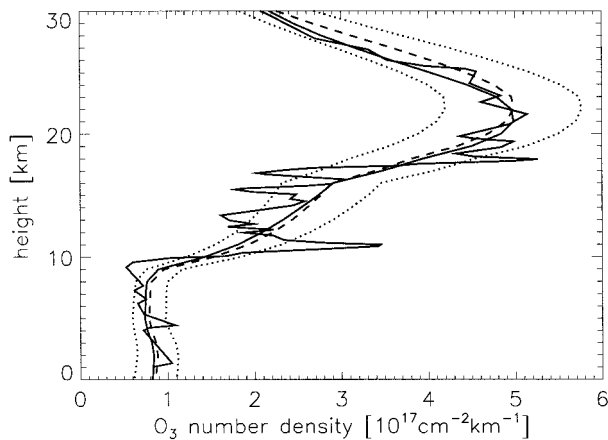


FIG. 14. GOME ozone profile and a collocated Hohenpeissenberg ozonesonde measurement (47.5°N, 11.0°E) on 21 March 1997 (Hoogen et al. 1998, manuscript submitted to *Phys. Chem. Earth*). The sonde profile is shown as a solid line and is highly structured (see laminated structure near 10-km altitude). The dashed line represents the GOME profile with the dotted lines indicating the  $1\sigma$  error. The smoothed solid line is the ozonesonde profile after convolving with the averaging kernels derived from the GOME retrieval (see text).

Fortuin and Kelder (1998, manuscript submitted to *J. Geophys. Res.*) based on combined sonde and satellite observations provides the a priori statistics for the retrieval. Figure 14 shows a comparison between a GOME vertical ozone profile and the results from a collocated ozone sonde launched in Hohenpeissenberg on 21 March 1997. An interesting observation is that GOME cannot resolve the narrow ozone peak centered near 10-km altitude as observed by the sonde. The full-width half maximum of the rows of the GOME averaging kernel matrix,

$$\mathbf{A}_i = \mathbf{S}^{-1} \mathbf{K}_i^T \mathbf{S}_y^{-1} \mathbf{K}_i, \quad (14)$$

approximately yields the vertical resolution of the retrieved GOME profiles. Convoluting the high-resolution sonde profiles with the averaging kernels reduces the vertical resolution of the sonde profiles to that of the GOME profiles. [Convolution equation is given by Eq. (8), when  $\mathbf{x}_i$  is replaced by the sonde profile and  $\mathbf{y} - \mathbf{y}_i$  is set to zero. The product of matrices left are then identical to the averaging kernel matrix.] Satisfactory agreement between the convolved sonde profiles and the GOME results can be seen in Fig. 14. A time series of sonde profiles from Hohenpeissenberg Observatory and collocated GOME profiles during the period from July 1996 to June 1997 are shown in Fig. 15. The seasonal variation with the observed winter/spring maximum in the lower stratosphere is well documented by the GOME profiles. Comparisons of GOME profiles with other European stations similar to Fig. 15 show that the GOME profiles tend to slightly overestimate the sonde profiles by up to 10% (Hoogen et al. 1998, manuscript submitted to *Phys. Chem. Earth*). The standard deviation of the differences between the sonde and

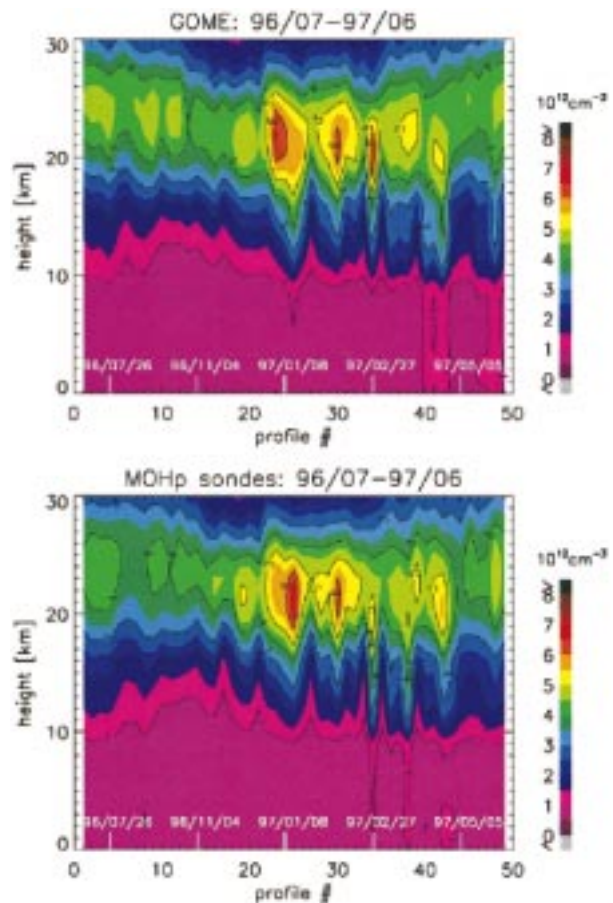


FIG. 15. Comparison of 49 sonde profiles with collocated measurements from GOME between July 1996 and June 1997 (Hoogen et al. 1998, manuscript submitted to *Phys. Chem. Earth*). GOME ozone profiles, top. Hohenpeissenberg sonde profiles after convolution with GOME averaging kernels, bottom.

GOME results is on the order of 10%–20% (Hoogen et al.) and considering that the accuracy and precision limit of sonde profiles is in the range of 5%–10% depending on altitude (Barnes et al. 1985), the agreement is reasonable. Some of the discrepancies can be explained by the differences in the air masses probed by GOME and the sondes. Since spectral information from GOME channel 1A ( $<307$  nm) are utilized in the retrieval, the surface area covered by the GOME profile is about  $100 \times 960$  km<sup>2</sup> (see Table 1). Particularly large gradients in the profiles are observed near the polar vortex edge. In those cases, where the vortex edge is close to the sonde stations, larger discrepancies are expected.

By extending the comparison to other sonde stations and other ground-based measurements such as lidars and microwave radiometers in addition to ozone profiles derived from other satellite sensors, for instance SAGE II, HALOE, and MLS, in the near future, a more detailed insight in the accuracy and precision of the GOME retrieval will be obtained. The first application of this GOME ozone profile retrieval was the derivation of

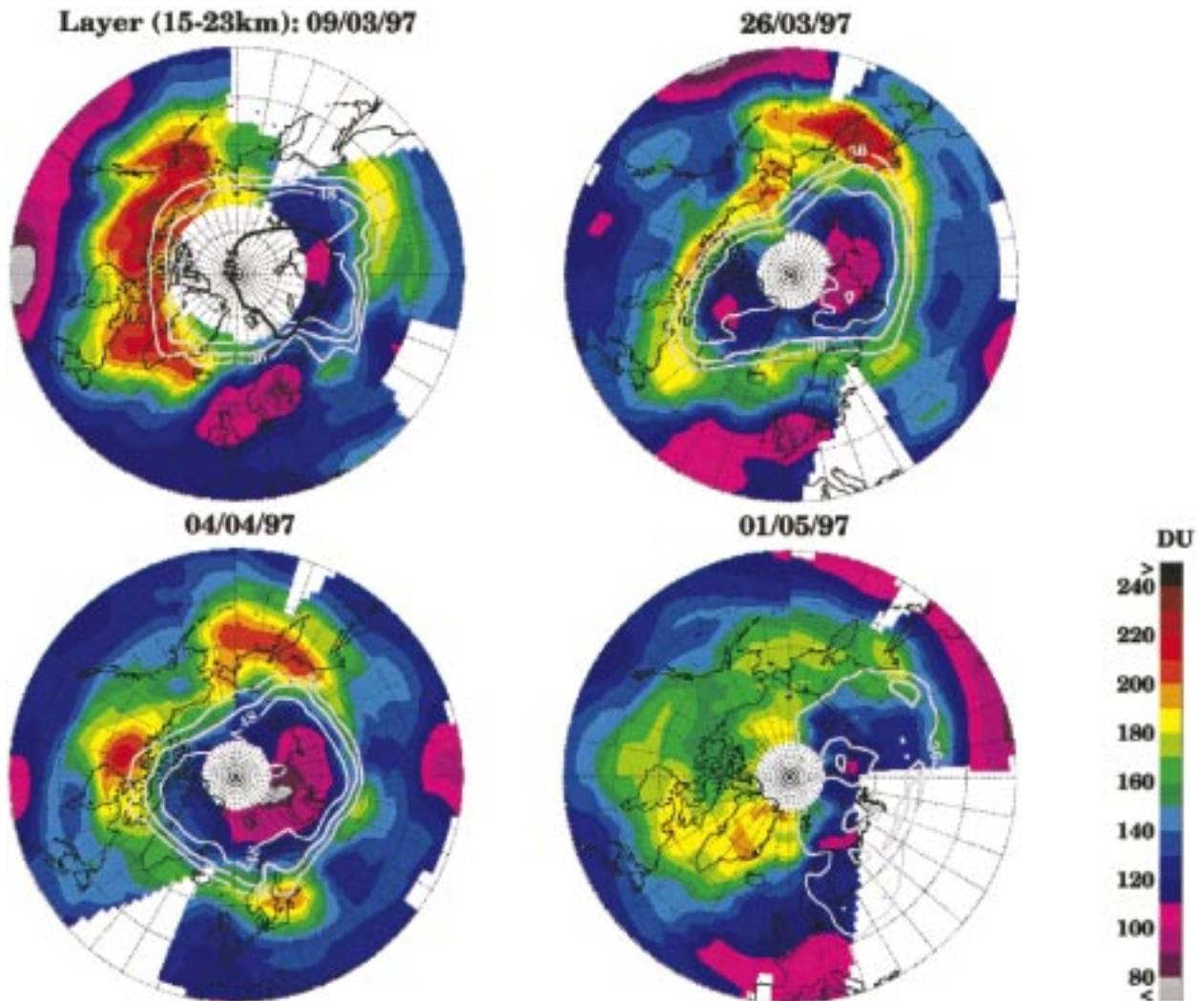


FIG. 16. Northern Hemispheric ozone distribution in the lower stratosphere (15–23 km) for four selected days during Arctic spring 1997: 9 March, 26 March, 4 April, and 1 May 1997. Polar vortex edge is indicated by the white contours of potential vorticity at 475 K in units of  $36, 42, \text{ and } 48 \times 10^{-6} \text{ K m}^2 \text{ kg}^{-1} \text{ s}^{-1}$ . Temperatures below the PSC formation point (194 K) are indicated by the black contour and have been observed on 9 March 1997. The meteorological analysis is from the European Centre for Medium-Range Weather Forecasts (ECMWF).

global ozone fields in the Northern Hemisphere during Arctic spring 1997 (Bramstedt et al. 1997; Eichmann et al. 1997, 1998). Ozone distributions for four days during the March–May 1997 period are shown for the low and middle stratosphere in Figs. 16 and 17, respectively. A reduction of approximately 50% of the polar vortex ozone as compared to the background levels outside the vortex has been observed by GOME in the low and middle stratosphere. In the low stratosphere the motion of an anticyclone across Europe is clearly seen on 9 and 26 March 1997, carrying low ozone from the subtropics into midlatitude regions. The exchange of air masses between the subtropical region and the mid- and polar latitudes occurs primarily in the low stratosphere. Height-resolved ozone distributions derived from GOME may, therefore, provide important information on the influence of atmospheric dynamics on the ozone

chemistry. This is particularly important in the Northern Hemisphere, where the meteorological variability is largest.

## 7. Conclusions

GOME is the first of a new generation of passive UV/visible/NIR remote sensing instruments, whose aim is to monitor atmospheric constituents related to the global change issue. The simultaneous observation of a wide spectral region at moderate spectral resolution enables column amount of several trace gases as well as aerosol, cloud, and surface parameters to be retrieved from the upwelling radiance measured at the top of the atmosphere (Koppers et al. 1997; Guzzi et al. 1997). GOME has successfully passed its initial validation phase and demonstrated its capability to provide valuable infor-

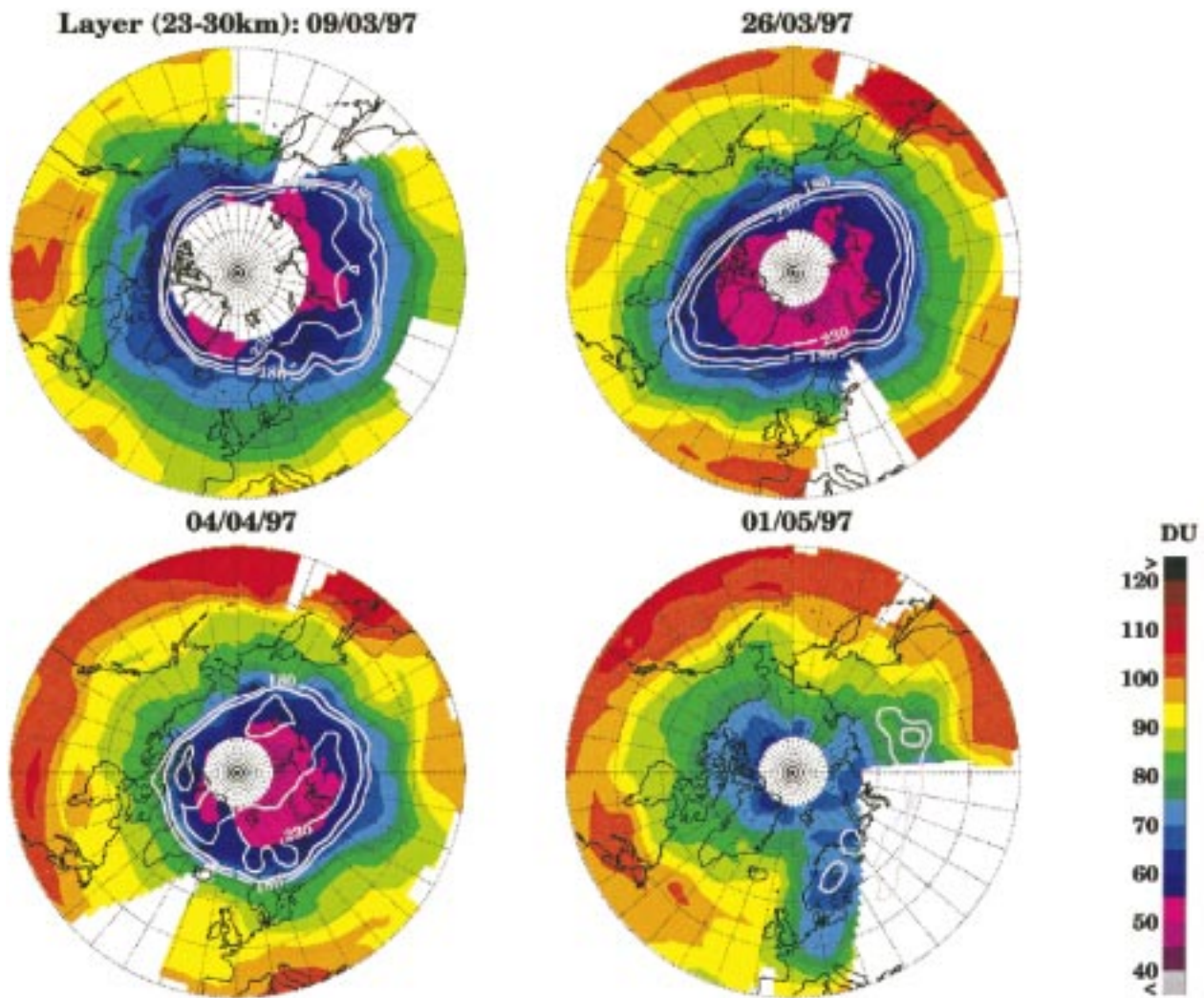


FIG. 17. Northern Hemispheric ozone distribution in the midstratosphere (23–30 km) for four selected days during Arctic spring 1997: 9 March, 26 March, 4 April, and 1 May 1997. Polar vortex edge is indicated by the white contours of potential vorticity at 675 K in units of 180, 205, and  $230 \times 10^{-6} \text{ K m}^2 \text{ kg}^{-1} \text{ s}^{-1}$ . The meteorological analysis is from the ECMWF.

mation about the state of the earth's atmosphere. In line with the experience gained from other space sensors, continuous improvement of the quality of the data is necessary and is an ongoing activity, which will enable GOME to make an optimal contribution to important and challenging issues such as long-term trend analysis of atmospheric composition. In addition, long-term variability in the solar UV irradiances due to the 11-year solar activity cycle, which may relate to observed cyclic fluctuations in the long-term trend of the annual global means of total ozone (Jackman et al. 1996) and, possibly, the global cloud cover (Svensmark and Friis-Christensen 1997), can be monitored using the daily solar GOME observations (Weber et al. 1998). The separation of natural and anthropogenic causes contributing to the global change issue is a challenging task. The series of new European UV/visible remote sensing instruments, starting with GOME on *ERS-2*, *SCIAMA-*

*CHY* on *ENVISAT* (launch in 2000), and the second generation GOME on the European operational meteorological satellite *METOP* (launch in 2002) will provide an important contribution to long-term continuity in global atmospheric measurements and monitoring.

*Acknowledgments.* We would like to express our thanks to the GOME project team at ESA/ESTEC, particularly A. Hahne, J. Callies, C. J. Readings, P. Dubock, and the GOME industrial team of Officine Galileo, Laben, TPD-TNO, Dornier Satellitensysteme, and British Aerospace. Without the support of a large international group of scientists from many international institutions, most notably, from the Royal Meteorological Institute of the Netherland (KNMI), the Smithsonian Astrophysical Observatory (SAO) (K. V. Chance), Belgian Institute of Space Aeronomy (BISA), Rutherford Appleton Laboratory (RAL), Space Research Organisation

Netherlands (SRON), University of Heidelberg, and the Max Planck Institute for Chemistry (MPIfC), who participated in the GOME Science Advisory Committee (GSAC), the GOME Data and Algorithm Subgroup (GDAS), the GOME Validation Subgroup, and the GOME Calibration and Characterization Subgroup, the success of the GOME mission would not have been possible. Particular thanks goes to the GOME ground segment team at the German Remote Sensing Data Center of the DLR led by W. Balzer and D. Loyola, and at ESA/ESRIN led by C. Zehner, who developed the GOME operational data processing and the instrument in-flight monitoring, respectively. Finally, we thank T. Kurosu, M. Vountas, and F. Wittrock (all University of Bremen) for their support. Parts of this work have been funded by the German Space Agency DARA (50EE9439, 50EE9440, and 50EP9207), ESA (11149/94/NL/CN and 12030/96/I-HGE), the State of Bremen, and the University of Bremen.

#### APPENDIX A

##### Availability of Data and Related Information

At the current stage level 2 data products (ozone and nitrogen dioxide vertical columns) and calibrated level 1 data products (earthshine radiance and solar irradiance) are available from the European Space Agency. Inquiries about the availability of GOME data products and ESA documents can be addressed to ESRIN ERS Helpdesk, ESA/ESRIN, via Galileo Galilei, I-00044 Frascati, Italy; Fax +39/6/94180510. Valuable information on GOME and near-real time data products can be also obtained on the Internet at the following addresses: <http://earth1.esrin.esa.it/eo/fr/eo4.63/eo4.96> (ESA/ESRIN); [http://auc.dfd.dlr.de/GOME/\(DFD/DLR\)](http://auc.dfd.dlr.de/GOME/(DFD/DLR)); [http://www.knmi.nl/onderzk/atmosam/GOME/\(KNMI\)](http://www.knmi.nl/onderzk/atmosam/GOME/(KNMI)); and <http://www.iup.physik.uni-bremen.de/> (University of Bremen).

#### APPENDIX B

##### Initial Cloud Fitting Algorithm (ICFA)

The ICFA algorithm estimates the cloud cover fraction contained in each single GOME ground pixel using channel 4 spectral reflectance measurements in the oxygen A band at 760 nm (see Fig. 2). The fractional cloud cover is estimated by determining the fractional contribution of the calculated oxygen transmittance from cloud-top pressure to top of atmosphere (TOA) and that from the ground. Since transmittance calculations using a line-by-line radiative transfer code are computationally expensive, the oxygen transmittances have been precalculated for some representative scenarios (solar zenith angle, line-of-sight, and cloud-top pressure) (Kuze and Chance 1994).

In the following the various steps in deriving the fractional cloud cover  $f$  will be described. The reflectance

measured at the TOA in the oxygen A band spectral range can be written as a sum of clear-sky and full cloud cover reflectances with the weight determined by the fractional cloud cover, that is,

$$R(\lambda) = fR_{\text{cld}}(\lambda) + (1 - f)R_{\text{grnd}}(\lambda) + P(\lambda). \quad (\text{B1})$$

The third term represents a closure term accounting for the continuum background, such that the  $R_{\text{cld}}$  and  $R_{\text{cfr}}$  are calculated reflectances in the presence of a cloud and without clouds, that is,

$$R_{\text{cld}}(\lambda) = a_{\text{cld}}(\theta, \theta_o) \int d\lambda' r(\lambda' - \lambda)T(\lambda', p_c, \theta, \theta_o) \quad (\text{B2})$$

and

$$R_{\text{grnd}}(\lambda) = A \int d\lambda' r(\lambda' - \lambda)T(\lambda', p_o, \theta, \theta_o), \quad (\text{B3})$$

where  $T(\lambda', p_c, \theta, \theta_o)$  and  $T(\lambda', p_o, \theta, \theta_o)$  are the spectral transmittances of the oxygen A band from TOA to the cloud top ( $p_c$ ) or the ground ( $p_o$  surface pressure) and reflected into the direction of the satellite line of sight. Here  $a_{\text{cld}}(\theta, \theta_o)$  is the bidirectional reflection coefficient for a given line of sight  $\theta$  and solar zenith angle  $\theta_o$  and  $A$ , the constant surface albedo. Also,  $r(\lambda' - \lambda)$  is the instrument response function, which has been measured for GOME and is well represented by the following form:

$$r(x' - x) = \frac{a_1^2}{(x' - x)^4 + a_o^2}, \quad (\text{B4})$$

where  $x$  and  $x'$  are detector pixel positions ( $x = 1, \dots, 1024$ ). The constant  $a_o$  has the values 0.8196, 0.6568, 0.7675, and 0.7377 in GOME channels 1, 2, 3, and 4, respectively, and  $a_1$  takes the values 0.8182, 0.6568, 0.7679, and 0.7381, respectively (ESA 1995, 64). The full-width half maximum of the response function is about 1.5 detector pixels.

If we define fitting constants  $\alpha_1 = fa_{\text{cld}}(\theta, \theta_o)$ ,  $\alpha_2 = (1 - f)A$ , and assume a linear background for  $P(\lambda)$  such that a linear regression of Eq. (B1) to measured reflectances is possible using precomputed oxygen transmittance templates, as given by the integrals in Eqs. (B2) and (B3). The fractional cloud cover is then determined either from  $\alpha_1$  or  $\alpha_2$  if the bidirectional cloud reflectivity or albedo, respectively, is taken from a database.

The transmission templates for the oxygen A band are calculated using line parameters from the HITRAN database (Rothman et al. 1998, manuscript submitted to *J. Quant. Spectrosc. Radiat. Transfer*). After dividing the atmosphere in plane-parallel layers, the transmittance  $T_k$  in the  $k$ th layer [pressure  $p_k$ ,  $\text{O}_2$  number density  $\rho(p_k)$ , vertical extent  $\Delta z_k$ ] can be defined as

$$\ln T_k(\lambda) \approx -\sigma(p_k, \lambda)\rho(p_k) \int_s ds. \quad (\text{B5})$$

The slant optical path for that layer is given by

$$\int_s ds = \Delta z_k(S_k(\theta_o) + 1/\cos\theta), \quad (\text{B6})$$

where  $\Delta z_k S_k(\theta_o)$  is the solar ray path through a refractive atmosphere [for small solar zenith angles  $S_k(\theta_o) \approx 1/\cos\theta_o$ ], and  $\sigma(p_k, \lambda)$  the oxygen absorption cross section. The total cumulative transmittance  $T$  is obtained by summing over all atmospheric layers above  $p_c$  or  $p_o$ , that is,

$$\ln T(\lambda) = \sum_{k=k_{\min}} -\sigma(p_k, \lambda)\rho(p_k)\Delta z_k(S_k(\theta_o) + 1/\cos\theta). \quad (\text{B7})$$

For the templates 16 lower boundary levels as indicated by  $k_{\min}$  have been selected, corresponding to 15 cloud-top pressures and surface pressure. The cumulative transmittance has been calculated for 11 001 data points between 12 780 and 13 220  $\text{cm}^{-1}$  (756.4–782.5 nm) at a spectral resolution of 0.04  $\text{cm}^{-1}$  ( $\sim 0.0025$  nm) for several TOA solar zenith angles, line-of-sight angles, and starting pressure levels. Intermediate transmittance values are interpolated before convolving with the instrument response function.

In the current ICFA implementation the actual cloud top pressure for a given geolocation is taken from the ISCCP climatology (Rossow and Schiffer 1991). An advanced cloud detection algorithm, which also takes advantage of the PMD information (see Fig. 3) and which shall derive, in addition to cloud cover, cloud-top pressures and, possibly, the optical depth, is currently in development (Kurosu et al. 1997).

#### APPENDIX C

##### Improved Ozone AMF in the UV

The most important assumption used by the standard DOAS approach outlined in section 3b is that the atmosphere is optically thin. However, in the 325–335-nm GOME UV fitting window the ozone absorption is quite strong and the ozone air mass factor shows a significant wavelength dependence at high solar zenith angles. The spectral structures of the AMF follow closely the inverse structures of the ozone absorption cross section. This wavelength dependence significantly increases with increasing solar zenith angle (see Fig. C1).

The modified DOAS (MDOAS) method outlined below accounts for the wavelength dependence of the AMF. However, this scheme was considered too computer time consuming to be implemented for the current version of the GOME data processor. In this section it is shown that the ozone AMF at 325 nm used for operational ozone retrieval from GOME can be considered

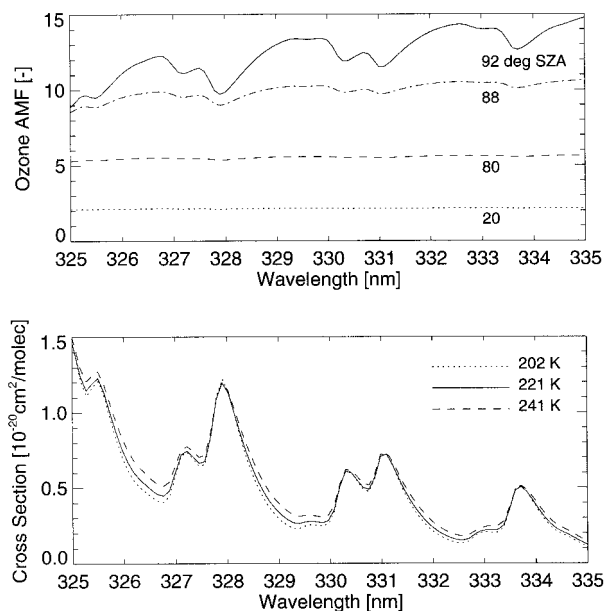


FIG. C1. Ozone air mass factor and cross section in the DOAS window 325–335 nm. (top) Ozone air mass factors for several solar zenith angles calculated with the radiative transfer program GOMETRAN. Scenario: nadir observation, albedo 10%, Jan 55°N MPI for Chemistry, 2D model profiles, and multiple scattering. (bottom) Ozone absorption cross section at three temperatures measured with the GOME flight model during the GOME on-ground calibration phase (Burrows et al. 1998b).

a good representative for the entire ozone DOAS fitting window, provided the solar zenith angle is not too large.

This result was obtained semiempirically by performing DOAS evaluations of synthetic spectra generated with the radiative transfer model GOMETRAN (Rozanov et al. 1997, 1998). For several scenarios (different solar zenith angles, ozone profiles, aerosol loadings, albedoes, etc.) ozone slant column densities (SCD) have been derived from the simulated spectra. The true AMF, defined as the AMF that exactly retrieves the (known) model ozone vertical column density (VCD), is simply the SCD derived from the DOAS fitting divided by the model VCD. This single AMF has been compared with the AMF spectrum calculated for the entire fitting window. In all cases the 325-nm AMF agreed to within 1%–2% with the true AMF, except for SZA above 80° where the error is generally larger. At 92° SZA this deviation might be as large as 6%.

On the contrary, using the AMF at the center wavelength (330 nm), the retrieved ozone VCD are always too low (deviation 2%–4% for SZA <70° and up to about 35% for SZA around 92°). Using the modified DOAS approach the model VCD could essentially be retrieved from the simulated measurements without any error even for an SZA of 92°. Figure C2 shows ozone total column retrieval errors for different choices of the AMF for the same model atmosphere as that used for Fig. C1.

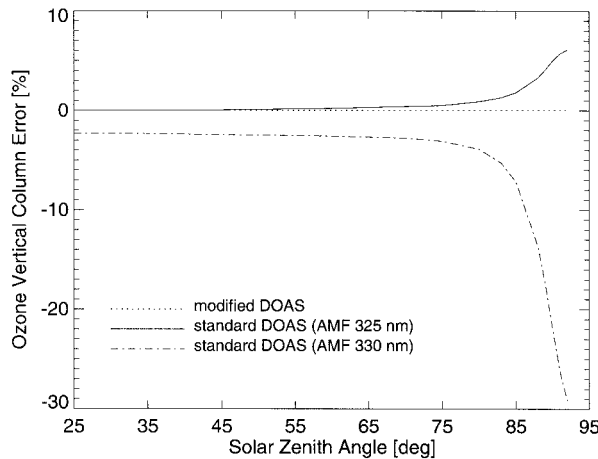


FIG. C2. DOAS vertical column retrieval error. Relative difference between ozone vertical column densities derived by applying the DOAS algorithm to simulated GOME measurements and the corresponding columns of the model atmosphere for different choices of the AMF.

The ozone absorption cross section in the 325–335-nm fitting window is strongest at 325 nm resulting in the smallest AMF at this wavelength. The surprising semiempirically derived result that the smallest AMF of the fitting window is generally the best representative single wavelength AMF for the entire window, shall be explained in the following. This important result has also been confirmed by DOAS ozone column retrievals in different spectral windows.

In order to understand how the AMF spectrum,  $\text{AMF}(\lambda)$ , for a given fitting window is mapped onto a representative single value  $\text{AMF}_{\text{rep}}$ , defined as the AMF that retrieves the known VCD in case of a perfect retrieval using simulated measurements, it would be most convenient for the interpretation of this mapping if the AMF spectral weighting function  $g(\lambda)$  is known. Therefore,  $\text{AMF}_{\text{rep}}$  shall be calculated as a scalar product between AMF vector  $\mathbf{a}$  and weights vector  $\mathbf{g}$  according to

$$\text{AMF}_{\text{rep}} = \sum_i g_i a_i \equiv \langle \mathbf{g}, \mathbf{a} \rangle, \quad (\text{C1})$$

with  $a_i \equiv \text{AMF}(\lambda_i)$  and  $g_i \equiv g(\lambda_i)$ .

The starting point for the calculation of  $\mathbf{g}$  is the modified DOAS equation in the following form:

$$\begin{aligned} \tau(\lambda, s) &\equiv -\ln\left(\frac{I(\lambda, s)}{F(\lambda)}\right) \\ &\approx -\text{VCD} \left[ \frac{1}{\text{VCD}_{\text{mod}}} \ln\left(\frac{I_{\text{mod}}(\lambda, s)}{F_{\text{mod}}(\lambda)}\right) \right] - P'(\lambda). \end{aligned} \quad (\text{C2})$$

The measured total slant optical density (SOD)  $\tau(\lambda, s)$ , defined as the negative logarithm of the measured earthshine radiance  $I(\lambda, s)$  divided by the solar irradiance  $F(\lambda)$ , is equated (apart from a scaling factor) with the corresponding model quantity minus a low-order polynomial in  $P'(\lambda)$  to subtract broadband features as in

standard DOAS. The scaling factor is the ratio of the VCD to be retrieved divided by the model VCD.

Equation (C2) can be transformed into the following equation, with  $I_{\text{mod,off}}$  calculated similarly to  $I_{\text{mod}}$ , except that the trace gas absorption of interest, here ozone, has been omitted, as follows:

$$\begin{aligned} \tau &\approx \text{VCD} \left[ \frac{1}{\text{VCD}_{\text{mod}}} \ln\left(\frac{I_{\text{mod,off}}}{I_{\text{mod}}}\right) - \frac{1}{\text{VCD}_{\text{mod}}} \ln\left(\frac{I_{\text{mod,off}}}{F_{\text{mod}}}\right) \right] - P' \\ &\approx \text{VCD} \left[ \frac{1}{\text{VCD}_{\text{mod}}} \ln\left(\frac{I_{\text{mod,off}}}{I_{\text{mod}}}\right) \right] - P \end{aligned} \quad (\text{C3})$$

(the wavelength dependence has been dropped). In case of one absorber only (this is essentially the case for the spectral window investigated here) the term  $\ln(I_{\text{mod,off}}/F_{\text{mod}})$  does not contain any absorptions and, therefore, is a smooth function of wavelength that can be absorbed in the subtracting polynomial  $P$ . Note that  $I_{\text{mod}}$  depends on the model ozone VCD. The differential ozone SOD, that is,  $\ln(I_{\text{mod,off}}/I_{\text{mod}})$  minus a polynomial, in general is assumed to scale with  $\text{VCD}_{\text{mod}}$ . If this is not true, the retrieved VCD depends on the assumed model VCD. This dependence is, in general, rather weak. If necessary, this problem can be solved using an iterative scheme. Convergence is achieved if the retrieved VCD essentially agrees with the  $\text{VCD}_{\text{mod}}$ . The profile shape, however, is assumed to be known as in standard DOAS.

In standard DOAS the fit parameter is the trace gas SCD, which is converted in a second step to the desired VCD by dividing the SCD by an appropriate AMF. In modified DOAS the (known) reference function is the trace gas SOD divided by the corresponding  $\text{VCD}_{\text{mod}}$ . The fit parameter is the trace gas VCD directly. The modified DOAS approach requires radiative transfer simulations for each spectral point in the fitting window (about 100 for the GOME 325–335-nm window). For standard DOAS the AMF needs to be calculated at one wavelength only.

It can be seen from Eq. (5) that the term  $\ln(I_{\text{mod,off}}/I_{\text{mod}})$ , that is, the model ozone SOD, corresponds to the wavelength dependent ozone air mass factor  $\text{AMF}(\lambda)$  as follows:

$$\frac{1}{\text{VCD}_{\text{mod}}} \ln\left(\frac{I_{\text{mod,off}}}{I_{\text{mod}}}\right) = \text{AMF}(\lambda)\sigma(\lambda), \quad (\text{C4})$$

if the altitude dependence of the cross section is neglected. The latter is the basic assumption made in standard DOAS retrieval. Rather than using the spectral AMF multiplied by the ozone absorption cross section as reference for the modified DOAS fitting [right-hand side of Eq. (C4)], the SOD can be used directly (left-hand side).

As the modified DOAS approach is able to retrieve accurate VCD, Eq. (C3) is a good starting point to determine the weights  $g_i$ . However, for this purpose, it is assumed that one representative absorption cross section  $\sigma(\lambda)$  can be defined (e.g., the cross section correspond-

ing to the temperature of the climatological number density profile maximum as in the operational GOME DOAS retrieval).

AMF<sub>rep</sub> can be determined by least squares minimization of the difference between the modified and the standard DOAS equation, that is,

$$\sum_i [AMF(\lambda_i)\sigma(\lambda_i) - AMF_{rep}\sigma(\lambda_i) - P(\lambda_i)]^2 = \min, \quad (C5)$$

with AMF<sub>rep</sub> and the coefficients of the polynomial  $P$  as fitting parameters. It can be shown that the solution of this problem can be written in the form of Eq. (C1) with

$$g_i = \frac{\langle \mathbf{X}\mathbf{P}\mathbf{x} \rangle_i}{\langle \mathbf{P}\mathbf{x}, \mathbf{x} \rangle}. \quad (C6)$$

Here  $\mathbf{x}$  is the wavelength-dependent ozone absorption cross section and  $\mathbf{X}$  is a diagonal matrix with  $X_{ii} \equiv x_i \equiv \sigma(\lambda_i)$ .  $\mathbf{P}$  is matrix  $\mathbf{1} - \mathbf{L}(\mathbf{L}^T\mathbf{L})^{-1}\mathbf{L}^T$  with  $L_{ij} \equiv \lambda_i^{j-1}$  and  $\langle \mathbf{X}\mathbf{P}\mathbf{x} \rangle_i$  is the  $i$ th component of vector  $\mathbf{X}\mathbf{P}\mathbf{x}$ .

However, AMF<sub>rep</sub> determined by Eqs. (C1) and (C6) does not exactly reproduce the same VCD as the modified DOAS approach (i.e., the correct VCD) as only a least squares minimization has been performed and exact agreement between the retrieved VCD with the VCD retrieved by the modified DOAS approach has not been required. This means that the SCD determined from the standard DOAS procedure divided by the representative AMF as given by Eq. (C1) does not exactly reproduce the correct VCD as is the case for modified DOAS.

It can be shown that the optimum representative AMF, AMF<sub>rep,opt</sub>, that is, the AMF that produces the same VCD as the modified DOAS approach, is given by

$$AMF_{rep,opt} = \frac{\langle \mathbf{x}, \mathbf{P}\mathbf{y} \rangle \langle \mathbf{X}\mathbf{a}, \mathbf{P}\mathbf{X}\mathbf{a} \rangle}{\langle \mathbf{x}, \mathbf{P}\mathbf{x} \rangle \langle \mathbf{X}\mathbf{a}, \mathbf{P}\mathbf{y} \rangle}, \quad (C7)$$

where  $\mathbf{y}_i \equiv \ln[I_{mod,off}(\lambda_i)/I_{mod}(\lambda_i)]$  is the simulated SOD.

Equation (C1) is much easier to interpret than Eq. (C7) as it directly gives the desired weights vector  $\mathbf{g}$ . The difference between AMF<sub>rep</sub> and AMF<sub>rep,opt</sub> is small (less than 1% for SZA below 90°).

The knowledge of  $\mathbf{g}$  now allows us to understand why the smallest AMF in the fitting window is a good representative for the entire window: vector element  $g_i$  describes how much  $a_i \equiv AMF(\lambda_i)$  contributes to AMF<sub>rep</sub>. It has to be noted that although the sum over all  $g_i$  equals unity, the elements of  $\mathbf{g}$  are not restricted to positive values. The most interesting point is that  $\mathbf{g}$  shown in Fig. C3 is strongly anticorrelated with  $\mathbf{a}$  and has even negative values where the local maxima of the AMF are. The weights  $g_i$  are largest where the AMF has (local or global) minima. This means that AMF<sub>rep</sub> is strongly weighted toward the smallest AMF in the fitting window. In general, AMF<sub>rep</sub> is close to, but not necessarily identical to, the smallest AMF in the window (from Figs. C2 and C3 it might be concluded that the AMF around 325.2 nm would be a better choice for SZA around 90°).

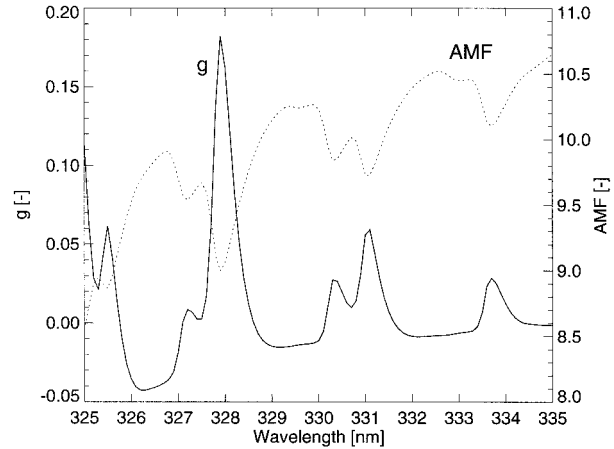


FIG. C3. Spectral AMF weights. Spectral AMF (dotted line) and corresponding weights (solid line) calculated for the same model atmosphere and viewing geometry as used for Figs. C1 and C2, a solar zenith angle of 88°, an ozone absorption cross section at 221 K, and a third-order polynomial.

Depending on the wavelength range selected for the DOAS fitting, it is even possible that AMF<sub>rep</sub> is smaller than the smallest AMF in the fitting window.

In conclusion, the outcome of this theoretical study is in agreement with the semiempirical results that the smallest AMF in the DOAS fitting window is actually a good representative for the UV window (325–335 nm) and a quantitative explanation for this is offered.

## REFERENCES

- Andreae, M. O., R. W. Talbot, T. W. Andreae, and R. C. Harris, 1988: Formic and acetic acid over the central Amazon region, Brazil. I. Dry season. *J. Geophys. Res.*, **93**, 1616–1624.
- Barnes, R. A., A. R. Bandy, and A. L. Torres, 1985: Electrochemical concentration cell ozonesonde accuracy and precision. *J. Geophys. Res.*, **90**, 7881–7887.
- Barrie, L. A., and Coauthors, 1988: Ozone destruction and photochemical reactions at polar sunrise in the lower Arctic atmosphere. *Nature*, **334**, 138–141.
- Barthia, P. K., R. D. McPeters, C. L. Mateer, L. E. Flynn, and C. Wellemeyer, 1996: Algorithm for the estimation of vertical ozone profiles from the backscattered ultraviolet technique. *J. Geophys. Res.*, **101**, 18 793–18 806.
- Bovensmann, H., J. P. Burrows, M. Buchwitz, J. Frerick, S. Noél, V. V. Rozanov, K. V. Chance, and A. P. H. Goede, 1999: SCIAMACHY: Mission objectives and measurement modes. *J. Atmos. Sci.*, **56**, 127–150.
- Bramstedt, K., and Coauthors, 1997: Ozone profiles from satellite data—Part II: First results from the Arctic winter campaign. *Proc. Fourth European Symp.*, Schliersee, Germany, European Commission, 189–192.
- Burrows, J. P., and K. V. Chance, 1993: GOME and SCIAMACHY: The scientific objectives, optical methods in atmospheric chemistry. *Proc. SPIE*, **1715**, 562–573.
- , —, P. J. Crutzen, H. van Dop, J. C. Geary, T. J. Johnson, G. W. Harris, I. S. A. Isaksen, G. K. Moortgat, C. Muller, D. Perner, U. Platt, J.-P. Pommereau, and H. Rodhe, 1988a: SCIAMACHY—A European proposal for atmospheric remote sensing from the ESA Polar Platform. Max Planck Institute for Chemistry, Mainz, Germany, 95 pp. [Available from Max-Planck-Institut für Chemie, P.O. Box 3060, D-55020 Mainz, Germany.]

- , and Coauthors, 1988b: SCIAMini. Max Planck Institute for Chemistry, Mainz, Germany, 80 pp. [Available from Max-Planck-Institut für Chemie, P.O. Box 3060, D-55020 Mainz, Germany.]
- , W. Schneider, and K. V. Chance, 1990: GOME and SCIAMACHY: Remote sensing of stratospheric and tropospheric gases. *Proc. 1st European Workshop*, Schliersee, Germany, European Commission, 99–102.
- , A. Dehn, B. Deters, S. Himmelmann, A. Richter, S. Voigt, and J. Orphal, 1998a: Atmospheric remote-sensing reference data from GOME: Part 1. Temperature-dependent absorption cross sections of NO<sub>2</sub> in the 231–794 nm range. *J. Quant. Spectrosc. Radiat. Transfer*, in press.
- , A. Richter, A. Dehn, B. Deters, S. Himmelmann, S. Voigt, and J. Orphal, 1998b: Atmospheric remote-sensing reference data from GOME: Part 2. Temperature-dependent cross sections of O<sub>3</sub> in the 231–794 nm range. *J. Quant. Spectrosc. Radiat. Transfer*, in press.
- Coy, L., E. R. Nash, and P. A. Newman, 1997: Meteorology of the polar vortex: Spring 1997. *Geophys. Res. Lett.*, **24**, 2693–2696.
- Cruzen, P. J., 1979: The role of NO and NO<sub>2</sub> in the chemistry of the troposphere and stratosphere. *Annu. Rev. Earth Planet. Sci.*, **7**, 443–472.
- , and Coauthors, 1985: Tropospheric chemical composition measurements in Brazil during the dry season. *J. Atmos. Chem.*, **2**, 233–256.
- de Beek, R., R. Hoogen, V. Rozanov, and J. P. Burrows, 1997: Ozone profile retrieval from GOME satellite data I: Algorithm description. *Proc. Third ERS Symp.*, Florence, Italy, ESA, 749–754.
- DLR, 1996a: GOME level 0 to 1 algorithms description. Tech. Note ER-TN-DLR-GO-0022 (Issue 4/A), DLR/DFD, Oberpfaffenhofen, Germany, 57 pp. [Available from Deutsches Zentrum für Luft- und Raumfahrt e. V.-Deutsches Fernerkundungsdatenzentrum, P.O. Box 1116, D-82230 Wessling, Germany.]
- , 1996b: GOME level 1 to 2 algorithms description. Tech. Note ER-TN-DLR-GO-0025 (Issue 2/A), DLR/DFD, Oberpfaffenhofen, Germany, 41 pp. [Available from Deutsches Zentrum für Luft- und Raumfahrt e. V.-Deutsches Fernerkundungsdatenzentrum, P.O. Box 1116, D-82230 Wessling, Germany.]
- Dobber, M., 1997: GOME moon measurements including instrument characterisation and moon albedo. *Proc. Third ERS Symp.*, Florence, Italy, ESA, 743–747.
- , A. P. H. Goede, and J. P. Burrows, 1998: Observations of the moon by GOME, radiometric calibration and lunar albedo. *Appl. Opt.*, in press.
- EC, 1997: European research in the stratosphere—The contribution of EASOE and SESAME to our current understanding of the ozone layer. EUR 16986, European Commission, 238 pp. [Available from Office for Official Publications of the European Communities, 2, rue Mercier, L-2985, Luxembourg.]
- Eichmann, K.-U., K. Bramstedt, M. Weber, V. Rozanov, R. de Beek, R. Hoogen, and J. P. Burrows, 1997: Ozone profile retrieval from GOME satellite data II: Validation and applications. *Proc. Third ERS Symp.*, Florence, Italy, ESA, 755–758.
- Eisinger, M., A. Richter, J. P. Burrows, and A. Piters, 1996a: Studies on DOAS ozone column retrieval from the UV and visible measurements of GOME. GOME Geophysical Validation Campaign, ESA-WPP-108, ESA/ESTEC, Noordwijk, the Netherlands, 161–173.
- , J. Burrows, and A. Richter, 1996b: Studies on the precision of GOME irradiance and radiance products and GOME measurements of OClO and BrO over Antarctica. GOME Geophysical Validation Campaign, ESA-WPP-108, ESA/ESTEC, Noordwijk, the Netherlands, 93–105.
- , —, —, and A. Ladstätter-Weissenmayer, 1997: SO<sub>2</sub>, OClO, BrO, and other minor trace gases from the Global Ozone Monitoring Experiment (GOME). *Proc. Third ERS Symp.*, Florence, Italy, ESA, 675–680.
- ESA, 1991: Report of the Earth Observation User Consultation Meeting. ESA SP-1143, ESA/ESTEC, Noordwijk, the Netherlands, 289 pp. [Available from ESA/ESTEC, Publications Division, P.O. Box 299, 2200 AG Noordwijk, the Netherlands.]
- , 1993: GOME interim science report. ESA SP-1151, ESA/ESTEC, Noordwijk, the Netherlands, 59 pp. [Available from ESA/ESTEC, Publications Division, P.O. Box 299, 2200 AG Noordwijk, the Netherlands.]
- , 1995: GOME users manual. ESA SP-1182, ESA/ESTEC, Noordwijk, the Netherlands, 200 pp. [Available from ESA/ESTEC, Publications Division, P.O. Box 299, 2200 AG Noordwijk, the Netherlands.]
- , 1996: GOME Geophysical Validation Campaign. Final Results Workshop Proceedings ESA-WPP-108, ESA/ESTEC, Noordwijk, the Netherlands, 268 pp. [Available from ESA/ESTEC, Publications Division, P.O. Box 299, 2200 AG Noordwijk, the Netherlands.]
- Farman, J. C., B. G. Gardner, and J. D. Franklin, 1985: Large losses of total ozone in Antarctica reveal seasonal ClO<sub>x</sub> and NO<sub>x</sub> interaction. *Nature*, **315**, 207–210.
- Fortuin, P., and H. Kelder, 1998: An ozone climatology based on ozonesonde data and satellite measurements. *J. Geophys. Res.*, in press.
- Grainger, J. F., and J. Ring, 1962: Anomalous Fraunhofer line profiles. *Nature*, **193**, 762–762.
- Guzzi, R., M. Cattani, M. Cervino, C. Levoni, and F. Torricella, 1997: Aerosol optical thickness from GOME data—Methodological approach and preliminary results. *Proc. Third ERS Symp.*, Florence, Italy, ESA, 687–691.
- Hausmann, M., and U. Platt, 1994: Spectroscopic measurements of bromine oxide and ozone in the high Arctic during Polar Sunrise Experiment 1992. *J. Geophys. Res.*, **99**, 25 399–25 413.
- Hegels, E., and Coauthors, 1998: Global distribution of atmospheric bromine oxide from GOME on the earth observing satellite ERS-2. *Geophys. Res. Lett.*, **25**, 3127–3130.
- Hoekstra, R. L., C. Olij, E. Zoutman, M. Le Kluse, and J. Callies, 1996: Validation of in-orbit calibration of GOME. GOME Geophysical Validation Campaign, ESA-WPP-108, ESA/ESTEC, Noordwijk, the Netherlands, 21–25.
- Hoogen, R., V. V. Rozanov, K. Bramstedt, K.-U. Eichmann, M. Weber, and J. P. Burrows, 1998: O<sub>3</sub> profiles from GOME satellite data—I: Comparison with ozone sonde measurements. *Phys. Chem. Earth*, in press.
- Houghton, J. T., G. J. Jenkins, and J. J. Ephraums, Eds., 1991: *Intergovernmental Panel on Climate Change: The IPCC Scientific Assessment*. University of Cambridge Press, 365 pp.
- Jackman, C. H., E. L. Fleming, S. Chandra, D. B. Considine, and J. E. Rosenfield, 1996: Past, present, and future modeled ozone trends with comparisons to observed trends. *J. Geophys. Res.*, **101**, 28 753–28 767.
- Joiner, J., P. K. Barthia, R. P. Cebula, E. Hilsenrath, R. D. McPeters, and H. Park, 1995: Rotational Raman scattering (Ring effect) in satellite backscatter ultraviolet measurements. *Appl. Opt.*, **34**, 4513–4525.
- Koppers, G. A. A., D. P. Murthugh, and J. Jansson, 1997: Aerosol optical thickness retrieval from GOME data in the oxygen A-band. *Proc. Third ERS Symp.*, Florence, Italy, ESA, 693–696.
- Kozlov, V., 1983: Design of experiments related to the inverse problem of mathematical physics. *Mathematical Theories of Experimental Design* (in Russian), C. M. Ermakov, Ed., Nauka Press, 216–245.
- Krueger, A. J., L. S. Walter, P. K. Barthia, C. C. Schnetzler, N. A. Krotkov, I. Sprod, and G. J. S. Bluth, 1995: Volcanic sulfur dioxide measurements from the Total Ozone Mapping Spectrometer instrument. *J. Geophys. Res.*, **100**, 14 057–14 076.
- , C. C. Schnetzler, and L. S. Walter, 1996: The December 1981 eruption of Nyamuragira volcano (Zaire), and the origin of the “mystery cloud” of early 1982. *J. Geophys. Res.*, **101**, 15 191–15 196.
- Kurosu, T., V. V. Rozanov, and J. P. Burrows, 1997: Parameterization schemes for terrestrial water clouds in the radiative transfer model GOMETRAN. *J. Geophys. Res.*, **102**, 21 809–21 823.

- Kuze, A., and K. V. Chance, 1994: Analysis of cloud top height and cloud coverage from satellite using O<sub>2</sub> A and B bands. *J. Geophys. Res.*, **99**, 14 481–14 491.
- Ladstätter-Weissenmayer, A., J. P. Burrows, A. Richter, F. Wittrock, M. Buchwitz, M. Weber, M. Eisinger, and R. Neuber, 1996: Validation of GOME O<sub>3</sub> and NO<sub>2</sub> measurements in Bremen, Ny-Alesund, and Neumayer. GOME Geophysical Validation Campaign, ESA-WPP-108, ESA/ESTEC, Noordwijk, the Netherlands, 153–160.
- Lambert, J.-C., and Coauthors, 1997: Validation of the ERS-2 GOME ozone products with the NDSC/alpine stations. *Proc. Third ERS Symp.*, Florence, Italy, ESA, 729–732.
- , M. Van Roozendaal, M. De Mazière, P. C. Simon, J.-P. Pomereau, F. Goutail, A. Sarkissian, and J. F. Gleason, 1999: Investigation of pole-to-pole performances of spaceborne atmospheric chemistry sensors with the NDSC. *J. Atmos. Sci.*, **176**–193.
- Lary, D. J., J. A. Pyle, and G. Carver, 1994: A three-dimensional model study of nitrogen oxides in the stratosphere. *Quart. J. Roy. Meteor. Soc.*, **120**, 453–482.
- Le Bras, G., and U. Platt, 1995: A possible mechanism for combined chlorine and bromine catalysed destruction of tropospheric ozone in the Arctic. *Geophys. Res. Lett.*, **22**, 599–602.
- McElroy, M. B., R. J. Salawitch, S. C. Wofsy, and J. A. Logan, 1986: Reductions of Antarctic ozone due to synergistic interactions of chlorine and bromine. *Nature*, **321**, 759–762.
- Müller, R., J.-U. Grooß, D. S. McKenna, P. J. Crutzen, C. Brühl, J. M. Russell III, and A. F. Tuck, 1997a: HALOE observations of the vertical structure of chemical depletion in the Arctic vortex during winter and early spring 1996–1997. *Geophys. Res. Lett.*, **24**, 2717–2720.
- , P. J. Crutzen, J.-U. Grooß, C. Brühl, J. M. Russell III, and H. Gernandt, and A. F. Tuck, 1997b: Severe chemical ozone loss in the Arctic during the winter of 1995–1996. *Nature*, **389**, 709–712.
- Naujokat, B., and S. Pawson, 1996: The cold stratospheric winters 1994/1995 and 1995/1996. *Geophys. Res. Lett.*, **23**, 3703–3706.
- Noxon, J. F., 1979: Stratospheric NO<sub>2</sub>, 2. Global behavior. *J. Geophys. Res.*, **84**, 5067–5076.
- , E. C. Whipple, and R. S. Hyde, 1979: Stratospheric NO<sub>2</sub>, 1. Observational method and behavior at mid-latitude. *J. Geophys. Res.*, **84**, 5047–5065.
- Platt, U., 1994: Differential optical absorption spectroscopy (DOAS). *Air Monitoring by Spectroscopic Techniques*, M. Siegrist, Ed., Chemical Analysis Series, Vol. 127, John Wiley and Sons, 27–84.
- Rex, M., and Coauthors, 1997: Prolonged stratospheric ozone losses in the 1995/96 Arctic winter. *Nature*, **389**, 835–838.
- Richter, A., F. Wittrock, M. Eisinger, and J. P. Burrows, 1998: GOME Observations of tropospheric BrO in northern hemispheric spring and summer 1997. *Geophys. Res. Lett.*, **25**, 2683–2686.
- Rodgers, C. D., 1976: Retrieval of atmospheric temperature and composition from remote measurements of thermal radiation. *Rev. Geophys. Space Phys.*, **95**, 5587–5595.
- , 1990: Characterization and error analysis of profiles retrieved from remote sounding measurements. *J. Geophys. Res.*, **95**, 5587–5595.
- , 1996: Information content and optimization of high-spectral resolution measurements. *Proc. SPIE*, **2830**, 136–147.
- Rossov, W. B., and R. A. Schiffer, 1991: ISCCP cloud data products. *Bull. Amer. Meteor. Soc.*, **72**, 2–20.
- Rothman, L. S., and Coauthors, 1998: The HITRAN molecular spectroscopic database and HAWKS (HITRAN atmospheric workstation). *J. Quant. Spectrosc. Radiat. Transfer*, in press.
- Roazanov, V. V., D. Diebel, R. J. D. Spurr, and J. P. Burrows, 1997: GOMETRAN: A radiative transfer model for the satellite project GOME—The plane parallel version. *J. Geophys. Res.*, **102**, 16 683–16 695.
- , T. Kurosu, and J. P. Burrows, 1998: Retrieval of atmospheric constituents in the UV/visible: A new analytical approach for the calculation of weighting functions. *J. Quant. Spectrosc. Radiat. Transfer*, **60**, 277–299.
- Sanders, R. W., S. Solomon, J. P. Smith, L. Perliski, H. L. Miller, G. H. Mount, J. G. Keys, and A. L. Schmeltekopf, 1993: Visible and near-ultraviolet spectroscopy at McMurdo Station, Antarctica. 9. Observations of OClO from April to October 1991. *J. Geophys. Res.*, **98**, 7219–7228.
- Santee, M. L., and Coauthors, 1996: Polar vortex conditions during the 1995–96 Arctic winter: MLS ClO and HNO<sub>3</sub>. *Geophys. Res. Lett.*, **23**, 3207–3210.
- , G. L. Manney, L. Froidevaux, R. W. Zurek, and J. W. Waters, 1997: MLS observations of ClO and HNO<sub>3</sub> in the 1996–97 Arctic polar vortex. *Geophys. Res. Lett.*, **24**, 2713–2716.
- Sessler, J., M. P. Chipperfield, J. A. Pyle, and R. Toumi, 1995: Stratospheric OClO measurements as a poor quantitative indicator of chlorine activation. *Geophys. Res. Lett.*, **22**, 687–690.
- Shannon, C., and W. Weaver, 1962: *The Mathematical Theory of Communication*. University of Illinois Press.
- Solomon, S., and R. R. Garcia, 1983: On the distribution of nitrogen dioxide in the high-latitude stratosphere. *J. Geophys. Res.*, **88**, 5229–5239.
- , A. L. Schmeltekopf, and W. R. Sanders, 1987: On the interpretation of zenith sky absorption measurements. *J. Geophys. Res.*, **92**, 8311–8319.
- Svensmark, H., and E. Friis-Christensen, 1997: Variation of cosmic ray flux and global cloud coverage—A missing link in solar-climate relationships. *J. Atmos. Terr. Phys.*, **59**, 1225–1232.
- Thuillier, G., M. Hersé, P. C. Simon, D. Labs, H. Mandel, and D. Gillotay, 1997: Observation of the UV solar spectral irradiance between 200 and 350nm during the ATLAS 1 mission by the SOLSPEC spectrometer. *Sol. Phys.*, **171**, 283–302.
- Vountas, M., V. V. Roazanov, and J. P. Burrows, 1998: Ring effect: Impact of rotational Raman scattering on radiative transfer in earth atmosphere. *J. Quant. Spectrosc. Radiat. Transfer*, in press.
- Wagner, T., and U. Platt, 1998: Satellite mapping of enhanced BrO concentrations in the troposphere. *Nature*, in press.
- Weber, M., J. P. Burrows, and R. P. Cebula, 1998: GOME solar UV/vis irradiance measurements between 1995 and 1997—First results on proxy solar activity studies. *Sol. Phys.*, **177**, 63–77.
- WMO, 1995: World Meteorological Organization, Scientific assessment of ozone depletion 1994. Rep. 37.